NEUROSCIENCE

Top-down modulation of the retinal code via histaminergic neurons of the hypothalamus

Rebekah A. Warwick[1]†, Serena Riccitelli[1]†, Alina S. Heukamp[1]‡, Hadar Yaakov[1]‡, Bani Prasad Swain[1], Lea Ankri[1], Jonathan Mayzel[1], Noa Gilead[2], Reut Parness-Yossifon[2], Stefano Di Marco[3,4], Michal Rivlin-Etzion[1]*

The mammalian retina is considered an autonomous circuit, yet work dating back to Ramon y Cajal indicates that it receives inputs from the brain. How such inputs affect retinal processing has remained unknown. We confirmed brain-to-retina projections of histaminergic neurons from the mouse hypothalamus. Histamine application ex vivo altered the activity of various retinal ganglion cells (RGCs), including direction-selective RGCs that gained responses to high motion velocities. These results were reproduced in vivo with optic tract recordings where histaminergic retinopetal axons were activated chemogenetically. Such changes could improve vision of fast-moving objects (e.g., while running), which fits with the known increased activity of histaminergic neurons during arousal. An antihistamine drug reduced optomotor responses to high-speed moving stimuli in freely moving mice. In humans, the same antihistamine nonuniformly modulated visual sensitivity across the visual field, indicating an evolutionary conserved function of the histaminergic system. Our findings expose a previously unappreciated role for brain-to-retina projections in modulating retinal function.

INTRODUCTION

The retina is typically viewed as an autonomous neuronal tissue, which processes external input—the visual image—and projects its output to the brain. Yet, more than a century ago, Ramon y Cajal showed that the avian retina is innervated by retinopetal axons coming from the brain via the optic nerve (*1*, *2*), suggesting that visual processing in the retina is subject to top-down modulations. Later, the presence of retinopetal axons was confirmed in various other vertebrate species, with some reports also in mammals, including humans [reviewed in (*3*)]. These studies described a few fibers that emerged from the optic disc and branched extensively to cover a large portion of the retina and tended to terminate in the inner plexiform layer (IPL) or the inner nuclear layer (*4*, *5*). Still, retinopetal axons in the mammalian retina remain elusive and their origin is controversial, probably due to the small number of projecting neurons.

Immunohistochemical analyses demonstrated the presence of retinopetal axons containing histamine in guinea pig, mouse, rat, and primate retinas (*6*–*10*). Because neurons located in the tuberomammillary nucleus (TMN) of the posterior hypothalamus are the only source of neuronal histamine in the mammalian nervous system (*10*–*13*), it was suggested that histaminergic retinopetal axons originate from the TMN (*14*). Moreover, it was explicitly shown that the retina does not contain any histamine-producing neurons (*14*), yet retinal histamine levels are comparable with other brain regions innervated by histaminergic neurons (*15*, *16*). Histaminergic axons generally do not form synaptic contacts, so histamine is thought to act in a paracrine fashion (*8*, *17*) via three types of histamine receptors (HRs) that have been identified in the mammalian CNS. H_1R and H_2R are G_q- and G_s-coupled receptors, respectively, and their direct action is usually excitatory, whereas H_3R is a G_i-coupled receptor that typically has an inhibitory effect (*17*). All three HRs were found in the retina (*15*, *16*), suggesting that histamine plays a neuromodulatory role in this tissue (*8*, *18*–*23*).

Histaminergic retinopetal axons pose a potential paradigm shift, as their existence suggests that higher brain areas can shape the retinal code. However, the functional role of histamine and its contribution to early visual processing is still poorly understood. Previous studies demonstrated that histamine acts on several retinal cell types, including cones, bipolar cells (BPs), and amacrine cells (ACs), via the activation of different receptors (*18*, *20*, *21*, *23*). Two studies found that histamine alters the output of a large portion of retinal ganglion cells (RGCs), but this effect was highly variable (*24*, *25*).

The firing rate of histaminergic neurons is correlated with the arousal state of the animal; they are minimally active during sleep and their activity peaks during attentive waking (*26*–*29*). It has recently been suggested that arousal state directly influences activity in early visual structures—the dorsal lateral geniculate nucleus (dLGN) and the superior colliculus (SC) (*30*, *31*), but it is unknown whether these effects are mediated by histamine or even retinopetal axons. To further complicate matters, histaminergic neurons are known to project to many brain areas, including those responsible for visual processing, raising the possibility that they locally modulate RGC axon terminals in these regions (*14*, *32*, *33*).

Here, we sought to reveal the effects of histaminergic retinopetal projections on retinal output. We first used viral injections in transgenic mice and identified histaminergic retinopetal projections that originate in the TMN. Using two-photon Ca^{2+} imaging, multielectrode array (MEA) and targeted patch clamp recordings, we showed that histamine affects both the baseline and light-evoked activity of various RGCs, including the OFF-transient alpha RGC and direction-selective ganglion cell (DSGC). Crucially, we demonstrated that both ex vivo histamine application and in vivo selective chemogenetic activation of the histaminergic retinopetal axons induce substantial changes in DSGCs, enhancing their responses to higher

[1]Department of Brain Sciences, Weizmann Institute of Science, Rehovot, Israel. [2]Ophthalmology Department, Kaplan Medical Center, Rehovot, Israel. [3]Center for Synaptic Neuroscience and Technology, Istituto Italiano di Tecnologia, Genova, Italy. [4]IRCCS Ospedale Policlinico San Martino, Genova, Italy.
*Corresponding author. Email: michal.rivlin@weizmann.ac.il
†These authors contributed equally to this work.
‡These authors contributed equally to this work.

motion velocities. Last, we found that an antihistamine reduces optomotor responses (OMRs) to fast-moving gratings in mice and affects visual sensitivity nonuniformly across the visual field in humans.

RESULTS

The retina is innervated by histaminergic fibers arising from the TMN of the hypothalamus

To confirm the presence of retinopetal axons and their origin, we unilaterally injected an adeno-associated virus (AAV) encoding for a fluorescent marker into the TMN of the posterior hypothalamus of wild-type mice (fig. S1A). After 4 to 6 weeks, we observed fluorescence in cell bodies in the TMN area. Immunostaining showed that some of these neurons were also positive for a specific marker for histaminergic cells, histidine decarboxylase (HDC), the enzyme that catalyzes the final step in the synthesis of histamine (fig. S1B). In addition to the labeled cell somas, we detected labeled axons in all regions known to be targeted by the TMN, including the retina, where few axons emerged from the optic disc and innervated the retina (fig. S1C). Using this approach, we also observed labeled cell bodies in the ganglion cell layer (GCL) of the retina, which possibly originated from retrograde labeling of RGC axons passing close to the injection site. Therefore, to ensure we specifically target histaminergic neurons, we switched to using HDC-Cre mice (see Materials and Methods).

The HDC-Cre mice experiments entailed injecting a Cre-dependent AAV encoding for a fluorescent marker into the TMN (Fig. 1A). Fluorescent cells were restricted to the TMN area and immunoreactive to HDC (Fig. 1B, 49.8 ± 3.0% of the HDC$^+$ neurons were transfected, mean efficiency ± SD, $n = 4$), validating the specificity of Cre-mediated recombination in HDC$^+$ cells (86.4 ± 11.6% of the transfected cells were HDC$^+$, mean specificity ± SD, $n = 4$, see Materials and Methods). Optic nerve whole mounts confirmed the presence of a few centrifugal fibers running through the optic nerve (Fig. 1C, red arrowheads). We also observed axons that seem to terminate in the optic nerve (Fig. 1C, red dashed line), but we cannot exclude the option that they reach the retina but are not detected by our approach. Notably, we found strongly labeled retinopetal axons in the retina that ran from the optic disc (Fig. 1D). Typically, these axons ran in the nerve fiber layer (NFL) and GCL and descended orthogonally into the IPL, where, despite being few in number, they branched extensively and covered a large portion of the retina, reaching the ora serrata (Fig. 1, D and E). The specificity of the virus

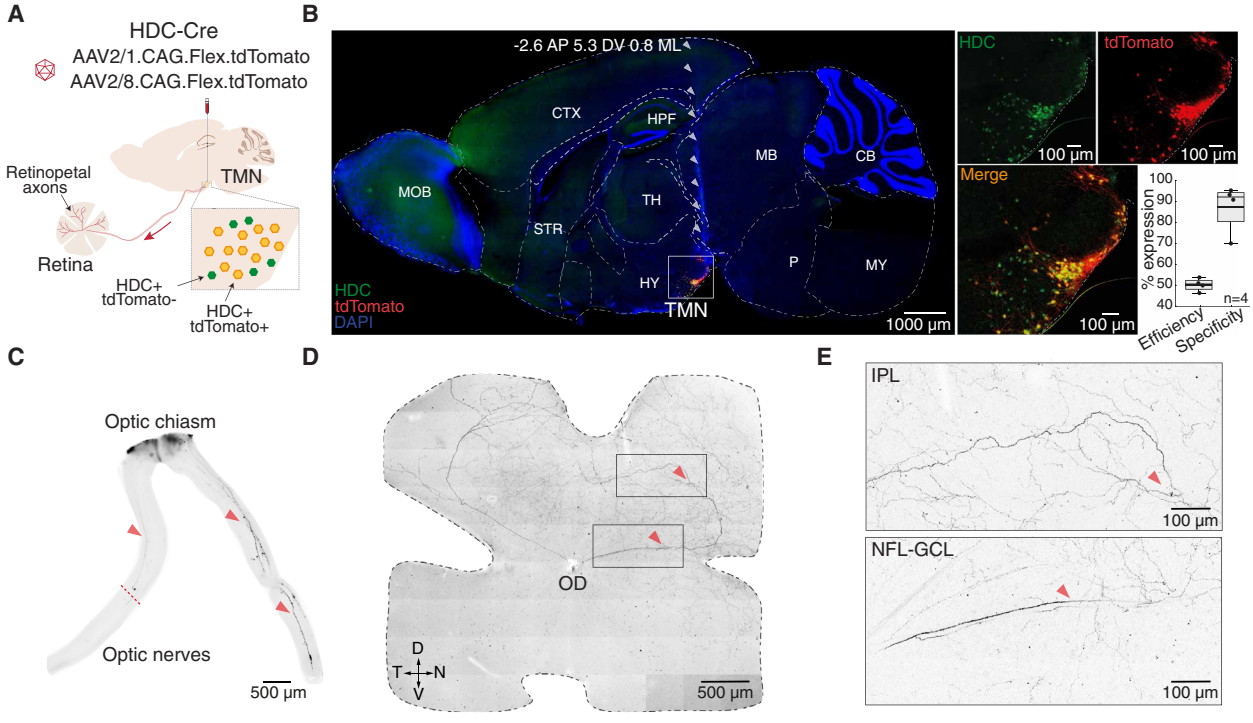

Fig. 1. Retinopetal histaminergic projections in HDC-Cre mice. (**A**) Microinjection of viral tracers in the TMN of transgenic mice expressing Cre in HDC$^+$ cells. Brains and retinas were analyzed after 4 to 6 weeks. (**B**) Left: sagittal brain slice of an HDC-Cre mouse 4 weeks after AAV2/8.CAG.Flex.tdTomato injection showing histaminergic neurons in the TMN area, identified by immunohistochemistry with HDC (green), also positive for tdTomato (red). Gray arrowheads indicate the injection trajectory. Right: High magnification of the TMN region indicated by the white box, with separated red and green channels (top) and merged (bottom left). Bottom right: quantification of the virus efficiency and specificity ($n = 4$ mice). Black and gray horizontal lines show the mean and median, respectively. Colored boxes represent the interquartile ranges. (**C**) Tiled fluorescence images showing histaminergic retinopetal axons in whole mount optic nerves. Red arrowheads indicate two positively labeled histaminergic fibers emerging from the optic chiasm (right). On the left, a dashed line indicates a fiber that terminates in the optic nerve. (**D**) Tiled fluorescence image of the retina (maximum intensity projection) showing two major fibers in the dorsal retina. The primary axons emerge from the optic disc. (**E**) High magnification of regions indicated by black boxes in (D). Top: Histaminergic axons branching in the IPL. Bottom: Histaminergic axon branches run through the NFL-GCL. Abbreviations: CTX, cortex; HPF, hippocampal formation; TH, thalamus; HY, hypothalamus; TMN, tuberomammillary nucleus; CB, cerebellum; MB, midbrain; P, pons; MY, medulla; MOB, main olfactory bulb; STR, striatum; IPL, inner plexiform layer; GCL, ganglion cell layer; NFL, nerve fiber layer; OD, optic disc; D, N, T, and V, dorsal, nasal, temporal, and ventral, respectively.

allowed us to unequivocally identify these retinopetal axons as histaminergic. In addition, it prevented the appearance of labeled neurons in the retina and allowed us to localize the histaminergic axons in the retinal layers. These results are in agreement with previous anatomical studies (*8*, *14*). The existence of histaminergic retinopetal projections suggests that retinal neurons can be subject to top-down neuromodulatory influences that act on the early stages of visual processing.

Histamine increases RGCs' baseline firing rates

Given that histaminergic axons innervate the retina, we sought to establish what effect, if any, histamine has on RGC firing rates. We used histamine concentrations ranging from 5 to 20 μM based on a dose-response curve (fig. S2) and previous studies (*18*, *20*, *21*, *23*–*25*). We used MEA recordings to systematically investigate the effect of histamine bath application on the baseline firing rate of spiking neurons in the RGC layer. We refer to these neurons as RGCs, although displaced spiking ACs can also be recorded (*34*). We found that 5 μM histamine caused 43.3 ± 16.4% (mean ± SD) of RGCs (seven retinas) to significantly increase their basal firing rate (Fig. 2, A to C). This was significantly more than in control experiments where histamine was not added. Only 1.2 ± 1.3% of RGCs showed reduced spiking activity upon histamine application. RGCs responsive to histamine included a variety of subtypes with ON, OFF, and ON-OFF polarity preferences, characterized by their response to a full-field stimulus presented before the addition of histamine (Fig. 2D).

Next, we conducted two-photon Ca^{2+} imaging of neurons in the RGC layer expressing GCaMP6f (referred to as RGCs hereafter). These experiments allow us to track single cells throughout the imaging session and identify RGCs based on response characteristics and soma size. Consistent with MEA results, the imaging data showed that histamine increased the intracellular Ca^{2+} concentration in 22.9 ± 9.6% and 23.7 ± 13.5% of RGCs (mean ± SD, four and six retinas) for 5 and 20 μM, respectively (Fig. 2, E and G). Blocking H_2R and H_3R did not change the percentage of RGCs that reacted to histamine, but any cocktail that included an H_1R blocker significantly reduced the percentage of responsive RGCs, showing that the

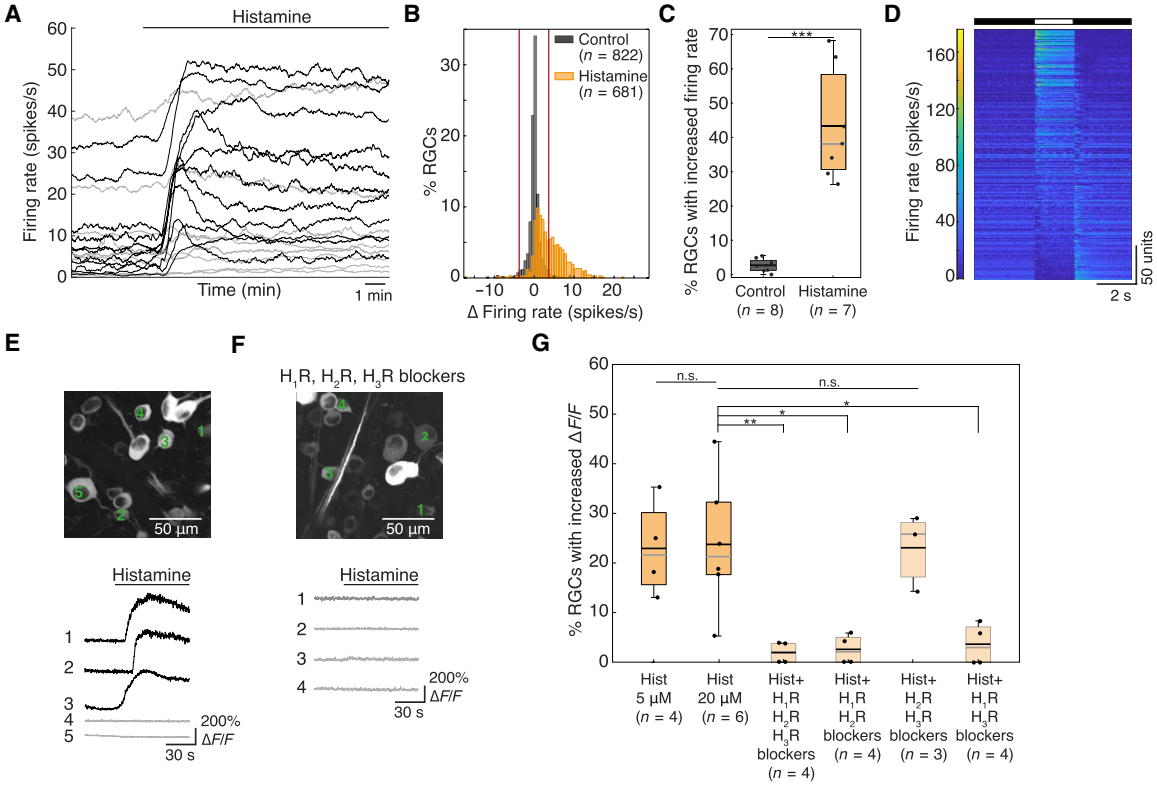

Fig. 2. Histamine increases the baseline activity of RGCs. (**A**) Baseline firing rates of example RGCs recorded on the MEA with bath application of histamine. Black cells significantly increased their firing rate upon the addition of 5 μM histamine application (horizontal black line above), while gray cells did not. (**B**) Distribution of the difference in firing rate compared to the baseline for control (no histamine added, black) and histamine (orange) experiments. Red vertical lines show upper and lower 2.5% quantile of control distribution. $P << 0.0001$, Kolmogorov-Smirnov test. (**C**) The proportion of RGCs that significantly increased their firing rate is significantly greater with histamine (orange, $n = 7$ retinas) than in the control (black, $n = 8$ retinas, $P = 0.0003$, one-tailed two-sample t test for unequal variances). (**D**) Responses to a full-field stimulus (indicated above) of all RGCs that increased their firing rate with histamine, sorted according to their ON-OFF preference, showing that various RGC types are responsive to histamine ($n = 319$ RGCs). (**E**) Top: Two-photon image of neurons in the ganglion cell layer of a Thy1-GCamp6f mouse. Bottom: Ca^{2+} traces of three RGCs that responded to histamine application (20 μM, black) and two RGCs that did not (gray). (**F**) Same as in (E) but in the presence of blockers of H_1R (cetirizine, 20 μM), H_2R (famotidine, 40 μM), and H_3R (JNJ 5207852, 20 μM). (**G**) Percentage of RGCs per retina that reacted to histamine ($\Delta F/F$ increased by more than 6 SDs relative to the baseline) when added alone (5 and 20 μM) or when histamine (20 μM) was added in the presence of various HR blocker combinations: $H_1R + H_2R + H_3R$ blockers, $P = 0.0099$; $H_1R + H_2R$ blockers, $P = 0.0107$; $H_1R + H_3R$ blockers, $P = 0.0120$, one-way Welch's ANOVA. (C and G), black and gray horizontal lines show the mean and median, respectively. Colored boxes represent the interquartile ranges. $*P < 0.05$, $**P < 0.01$, $***P < 0.001$; n.s., not significant.

effect of histamine on baseline activity of RGCs is mainly mediated by the H_1R (Fig. 2, F and G). The reaction times of different RGCs differ within the same experiment (Fig. 2E). The SD of the reaction time in each experiment fell between 5.8 and 9.6 s with an average of 7.6 s ($n = 6$ experiments, 20 μM histamine). This may be caused by varying expression levels of HRs (see the "Gene expression of H_1R is selective for DSGC" sections). Of note, by separating the data obtained from bath application of histamine (Fig. 2) based on retinal location, we found no differences in the proportion of RGCs that significantly increased their baseline activity between dorsal and ventral retinas (fig. S3).

Histamine changes the light responses of specific RGC subtypes

As histamine affects the baseline activity of RGCs, we investigated whether histamine modulates RGC responses to visual stimuli. Using two-photon Ca^{2+} imaging of the RGC layer, we characterized light responses of RGCs to an ultraviolet (UV) spot centered on the field of view (fig. S4). The mouse retina contains cones expressing short-wavelength opsin and is therefore responsive to UV light (*35*, *36*). RGCs were classified as either ON, OFF, or nonresponsive based on their Ca^{2+} transients (see Materials and Methods). Control experiments were undertaken in which histamine was not added. As the responses of some RGCs changed with time, only RGCs that kept their polarity preference (ON, OFF, or nonresponsive) in the pre- and washout conditions were included. The light response of most RGCs remained stable upon histamine application (20 μM). However, 27.5% of RGCs either lost, gained, or changed their polarity preference to the spot stimulus (76 of 276 RGCs, 22 retinas) compared to only 3% in the control dataset (3 of 98 RGCs, 7 retinas; fig. S4, A to E). Moreover, some of the RGCs that did not change their polarity preference exhibited an increase or decrease in their response amplitude (fig. S4B). Using the same dataset, we were able to identify putative ON-sustained alpha, OFF-sustained alpha, and OFF-transient alpha RGCs by selecting RGCs whose cell somas were greater than 20 μm in diameter. From these data, it appears that the ON- and OFF-sustained alpha RGCs retained their light responses, whereas OFF-transient alpha RGCs had overall diminished light responses (fig. S4, F to H).

To investigate this further, we conducted cell-attached recordings and targeted specific RGC subtypes, including alpha RGCs (see Materials and Methods). ON-sustained alpha RGCs were unaffected by the application of histamine (20 μM). These cells' background firing rates and light responses to spot stimuli remained unaltered by histamine (Fig. 3, A_i to E_i). The light-evoked responses of OFF-sustained alpha RGCs also appeared unaffected by histamine; however, an increase in their background firing rates was observed (Fig. 3, A_{ii} to E_{ii}). OFF-transient alpha RGCs increased their background activity after histamine was added, which made inhibition at light onset more apparent (Fig. 3, A_{iii} to C_{iii}). In addition, the maximum firing rate was significantly reduced for OFF-transient alpha RGCs when presented with larger spots, as were their response durations for smaller spots (Fig. 3, D_{iii} and E_{iii}). Last, we targeted ON-OFF posterior preferring direction-selective ganglion cells (pDSGC) using the transgenic Trhr-EGFP mouse line (see Materials and Methods). pDSGCs visibly increased their background firing rates upon histamine application (Fig. 3, A_{iv} and C_{iv}). The pDSCGs' light responses to spots were poor compared to those of the alpha RGC subtypes and tended to be further diminished by histamine (Fig. 3, B_{iv}, D_{iv}, and E_{iv}). However, this reduction was only significant for the OFF-response duration (Fig. $3E_{iv}$).

Gene expression of H_1R is selective for DSGCs

In light of the varied effects of histamine application on different retinal circuits, we aimed to identify the loci of histamine action by analyzing the expression levels of HRs in different cell types of the mouse retina. Analyses of previously published transcriptomic datasets (*37*–*39*) showed the presence of *Hrh1* and *Hrh3*, mRNA transcripts for H_1R and H_3R, in RGCs, while BPs and ACs primarily express *Hrh3* (fig. S5). *Hrh2* (transcripts for H_2R) displayed consistently low expression levels in RGCs, BPs, and ACs.

While *Hrh3* appeared to be uniformly expressed across all RGC clusters, *Hrh1* was predominant in a subset of RGCs (fig. S5, A to C), corroborating the role of H_1R as the primary receptor responsible for the baseline activity increase in a portion of RGCs (Fig. 2G). In line with our results, we observed that *Hrh1* mRNA expression in the 12_ooDS_NT cluster, to which pDSGCs likely belong due to its unique *Trhr* positivity (fig. S5C), was among the highest compared with all RGC clusters. Specifically, the *Hrh1* expression level in this cluster was significantly higher compared with clusters 42 and 43, which corresponds to OFF- and ON-sustained alpha RGCs, respectively, whereas it was not compared to cluster 45 corresponding to OFF-transient alpha RGC ($P = 0.0007$, $P = 0.0004$, and $P = 0.195$ for Kruskal-Wallis test with Dunn's post hoc correction for multiple comparisons, respectively). These data are in line with our targeted recording experiments and suggest that histamine acts directly on pDSGCs and OFF-transient alpha RGCs. Despite the low expression levels of *Hrh1* in OFF-sustained alpha RGCs, histamine did increase their baseline firing rate, probably because their high resting potential increases their sensitivity (*40*). We speculate that these cells were not significantly affected during stimulus presentation, because inhibitory conductance dominates the light responses of OFF-sustained alpha RGCs (*40*, *41*).

To further investigate this, we focused on DSGCs and their presynaptic cells. We found that the relatively high *Hrh1* mRNA expression was not specific to the 12_ooDS_NT cluster but found across other types of ON-OFF DSGCs as well as ON DSGCs, suggesting that histamine acts directly on multiple DSGC subtypes (fig. S5, A to C). Moreover, upstream BPs and ACs probably contribute no or very little to the histamine-induced changes in DSGCs: *Hrh1* mRNA levels were below detection thresholds in BCs in one dataset enriched with BCs (*38*) (fig. S5, D and E) and at very low levels in another (*42*). Starburst amacrine cells (SACs), the other major presynaptic cell to DSGCs, showed no *Hrh1* mRNA transcripts in any of the published datasets (*39*, *42*) (fig. S5, F and G). To further validate this hypothesis, we carried out voltage-clamp recordings from pDSGCs (clamped at −60 mV) and found that the current required to hold the cell on the target potential increased after histamine application, while no significant changes were detected in the frequency and amplitude of mini EPSCs (mEPSCs), supporting the idea that histamine acts directly on DSGCs to increase their excitability (*17*) (fig. S6).

Histamine enhances DSGCs' responses to high motion velocities

The finding that DSGCs are among the RGCs with the highest expression of *Hrh1*, combined with our results that histamine changes pDSGCs' responses to stationary spot stimuli, led us to investigate

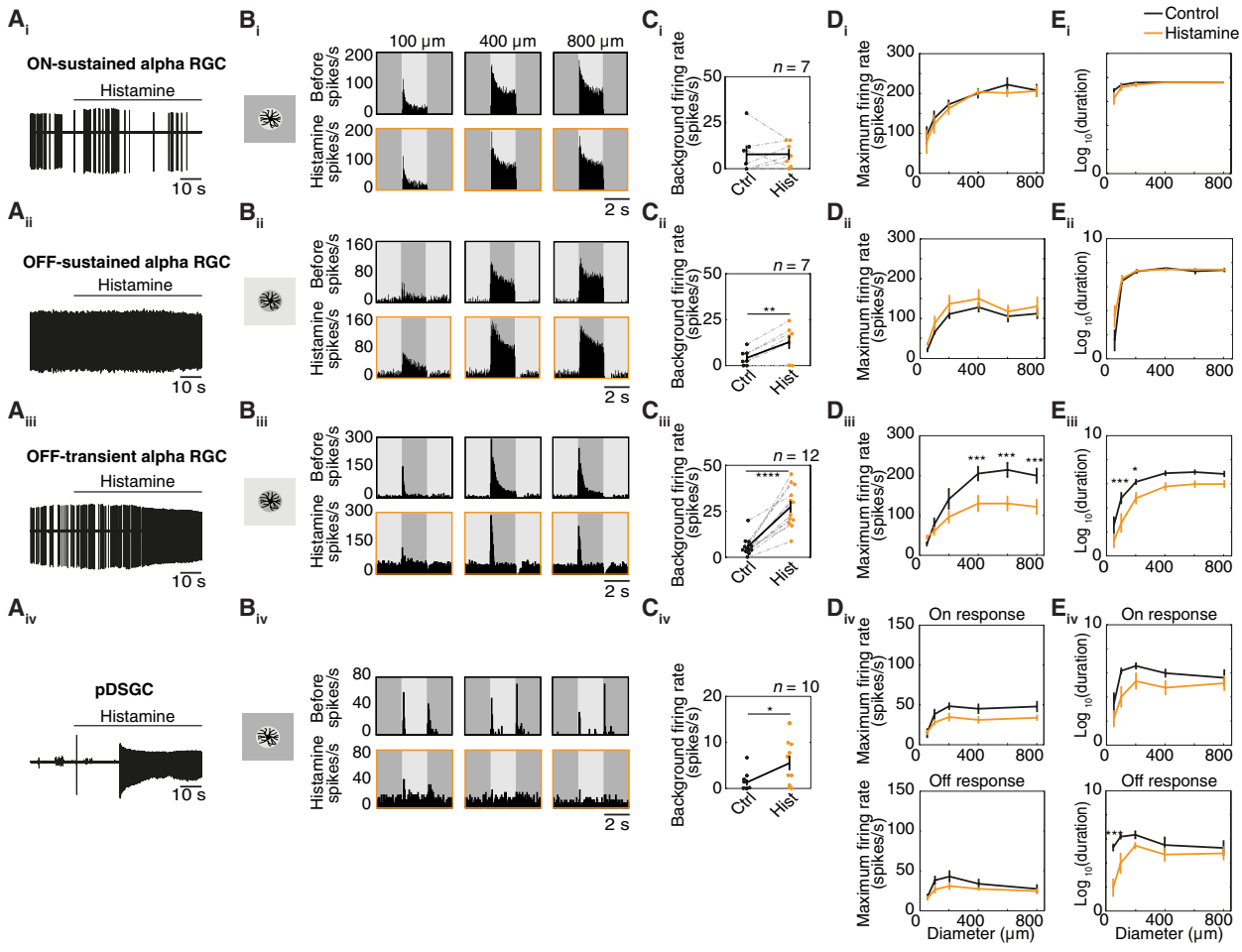

Fig. 3. Histamine changes the baseline activity and light responses of specific RGC subtypes. (**A**) Example traces (cell-attached recordings) of spiking activity of an ON-sustained alpha RGC (A_i), OFF-sustained alpha RGC (A_{ii}), OFF-transient alpha RGC (A_{iii}), and pDSGC (A_{iv}) upon the addition of 20 µM histamine. (**B**) PSTHs of example RGCs showing their light responses to different sized spots (100, 400, and 800 µm) before (top, black) and after (bottom, orange) histamine application. (**C**) Background firing rates (averaged over 2 s before the appearance of the spot) before and after histamine application for the different RGC subtypes. Bold line indicates the mean ± SEM, gray lines indicate paired cells. $P = 0.0085$ for (C_{ii}), $P < 0.0001$ for (C_{iii}), paired *t* test; $P = 0.0231$ for (C_{iv}), independent-sample *t* test. (**D** and **E**) Population data of the maximal firing rate (D) and response duration (log scale) (E) to different sized spots (mean ± SEM). (D_{iii}) 200 µm, $P = 0.0389$; 400, 600, and 800 µm, $P < 0.0001$. (E_{iii}) 100 and 200 µm, $P = 0.0003$ and 0.0346, respectively. (E_{iv}) 50 and 100 µm, $P = 0.0003$ and $P = 0.0314$, respectively. Two-way repeated-measures ANOVA with Bonferroni post hoc correction for multiple comparisons. *$P < 0.05$, **$P < 0.01$, ***$P < 0.001$, ****$P < 0.0001$.

whether histamine also alters their responses to moving stimuli. Because locomotion velocity is a common measure for arousal (*43*) and given that histaminergic neurons are known to increase their firing rate with arousal, we hypothesized that histamine shifts the velocity tuning of DSGCs to favor higher velocities resulting from increased running speed. To test this, we patch-clamped pDSGCs, recorded in cell-attached mode, and presented them with moving gratings at various temporal frequencies, ranging from 1 to 10 Hz (corresponding to 400 and 4000 µm/s or 13.3° and 133°/s, respectively). We assessed their responses before and after histamine application (10 µM). In contrast to pDSGCs' poor light responses to static spot stimuli, they exhibited robust light responses to moving stimuli and maintained their preferred posterior direction after histamine application (Fig. 4, A to D).

In control conditions, pDSGCs exhibited high discharge rates in response to slow-moving gratings (1 to 2 Hz) and diminished or no responses to faster-moving gratings (4 to 10 Hz; Fig. 4, A to C). Upon histamine application, pDSGCs improved their ability to encode faster-moving stimuli as is evident by the significant increase in the normalized response in the preferred direction (PD) at 6 and 8 Hz, while maintaining direction selectivity at these high motion velocities (Fig. 4, A to D). This increase in firing rate was not merely a by-product of the increased baseline activity, because the responses were time-locked to the grating stimulus (Fig. 4B). Although direction selectivity was maintained, we did notice a trend indicating a broader tuning (i.e., lower gDSI) at slower speeds (Fig. 4D). This overall broadening of pDSGCs after histamine application was verified in a different dataset where only slow-moving gratings and bars were presented (fig. S7).

Because high *Hrh1* mRNA expression is found in multiple DSGC subtypes and is not exclusive to the pDSGCs (fig. S5, A to C), we expanded our investigation to a larger dataset containing different subtypes of DSGCs obtained through MEA recordings. For the 27 of 385 RGCs classified as DSGCs (see Materials and Methods), we

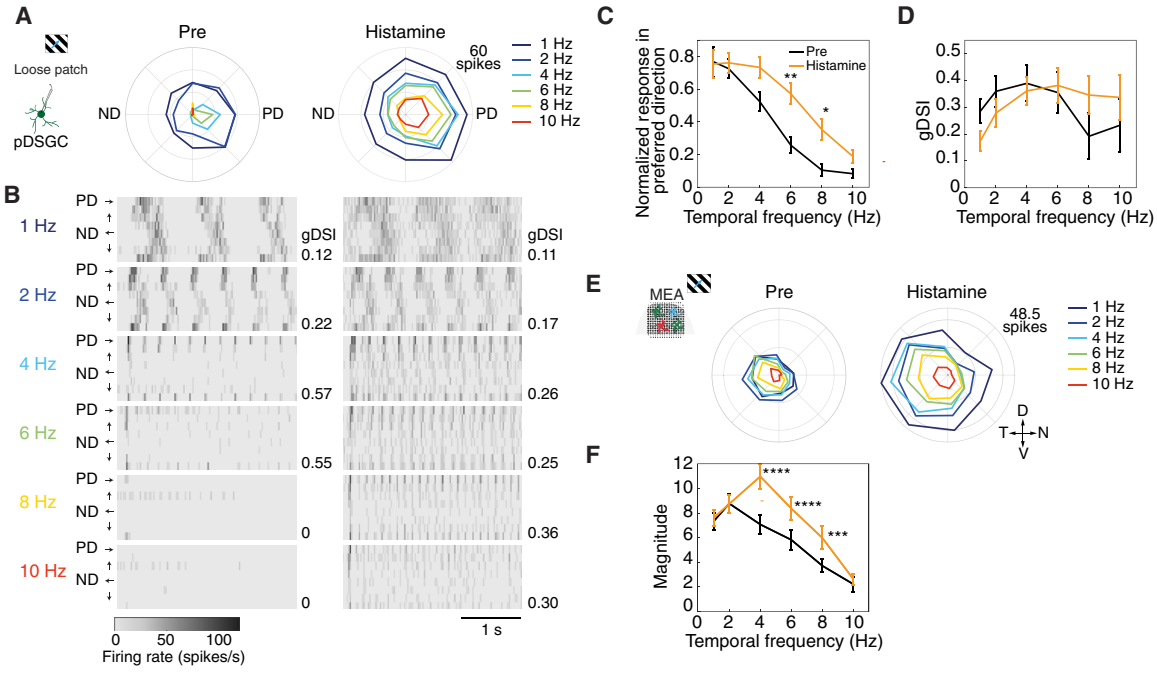

Fig. 4. Histamine enhances DSGCs' responses when presented with higher velocity stimuli. (**A**) Polar plots showing the responses of an example pDSGC to moving gratings at different temporal frequencies, obtained using patch clamp recordings, before (left) and after 10 μM histamine application (right). Colors denote temporal frequencies. (**B**) Heatmaps showing the mean firing rate of the cell in (A) in response to gratings moving at different temporal frequencies denoted on the left, before (left) and after (right) histamine application. Each row within each subplot corresponds to one of eight different directions of the grating stimulus [four depicted by the arrows; PD and ND according to (A)]. gDSIs are denoted on the right. (**C** and **D**) Population data (mean ± SEM) of the normalized response in the preferred direction (C, $P = 0.0013$ for 6 Hz and $P = 0.025$ for 8 Hz) and gDSI (D). $n = 9$ to 11 cells for each frequency. Before (pre) and after histamine conditions are shown in black and orange, respectively. (**E**) Same as (A) for a representative DSGC recorded on the MEA. (**F**) First harmonic magnitude of the FFT at the stimulus frequency as a function of temporal frequency for all DSGCs recorded on the MEA ($n = 27$; $P < 0.0001$, $P < 0.0001$, and $P = 0.0001$ for 4, 6 and 8 Hz, respectively). Two-way repeated-measures ANOVA with Bonferroni post hoc correction for multiple comparisons. Abbreviations: D, dorsal; N, nasal; V, ventral; T, temporal; PD, preferred direction; ND, null direction. *$P < 0.05$, **$P < 0.01$, ***$P < 0.001$, ****$P < 0.0001$.

calculated the first harmonic magnitude (extracted at the stimulus frequency) computed by fast Fourier transform (FFT) of the mean PSTH in response to the PD motion. We observed a significant increase in the FFT magnitude for responses to gratings moving at 4, 6, and 8 Hz after histamine application (Fig. 4, E and F). Together, these findings show that histamine extends the range of motion velocities that DSGCs can encode, enabling them to track faster-moving stimuli in a time-locked manner.

We used HR blockers to investigate which specific receptors are responsible for improving DSGCs' ability to track fast motion stimuli. We repeated the patch-clamp recordings (2, 6, and 8 Hz) in the presence of the H_1R blocker (cetirizine, 50 μM) and found that responses to 6 and 8 Hz remained unaltered by histamine (fig. S8, A to C). However, when H_2R (famotidine, 50 μM) and H_3R (JNJ 5207852, 20 μM) were blocked, histamine application (10 μM) significantly increased pDSGCs responses in the PD at 6 and 8 Hz, suggesting that it is the H_1R that mediates histamine's enhancement of pDSGCs' responses to high motion velocities, in line with the transcriptomic data (figs. S8, D to F, and S5).

Histaminergic neurons modulate the activity of DSGCs to track faster-moving stimuli in vivo

To further demonstrate the role of histaminergic retinopetal axons in shaping early visual processing, we recorded RGC axons in the optic tract in anesthetized mice using a Neuropixels probe before and after chemogenetically activating histaminergic retinopetal axons. We injected, 3 to 4 weeks before the experiment, an AAV2/8.hSyn.DIO.hM3D(Gq).mCherry, which drives the expression of the hM3Dq receptor (Gq-coupled human M3 muscarinic DREADD) in a Cre-dependent manner, into the TMN of HDC-Cre mice [hereafter referred to as hM3Dq (see Materials and Methods)]. Recording in the optic tract allows us to record RGC activity in vivo before any local modulation can occur on RGC axonal terminals and also excludes potential effects of histaminergic modulation on higher visual areas (*11*, *32*). A total of six experiments were conducted, three control and three hM3Dq (Fig. 5, A and B). In all experiments, the mice were presented with moving gratings with temporal frequencies of 2, 4, and 8 Hz (corresponding to 26.6°, 53.2°, and 106.4°/s) before and after clozapine-N-oxide (CNO) injection, which activates the hM3Dq receptor (*44*–*47*). In total, we identified 25 of 188 (13.3%) and 48 of 284 (16.7%) optic tract units that were DS in control and hM3Dq mice before CNO application, respectively (example cells in Fig. 5, C to F and H to K). Similar to the MEA histamine experiments, we examined the first harmonic magnitude (extracted at the stimulus frequency) computed by FFT of the mean PSTH in response to the PD motion (see Materials and Methods). We observed a significant increase in the FFT magnitude for responses

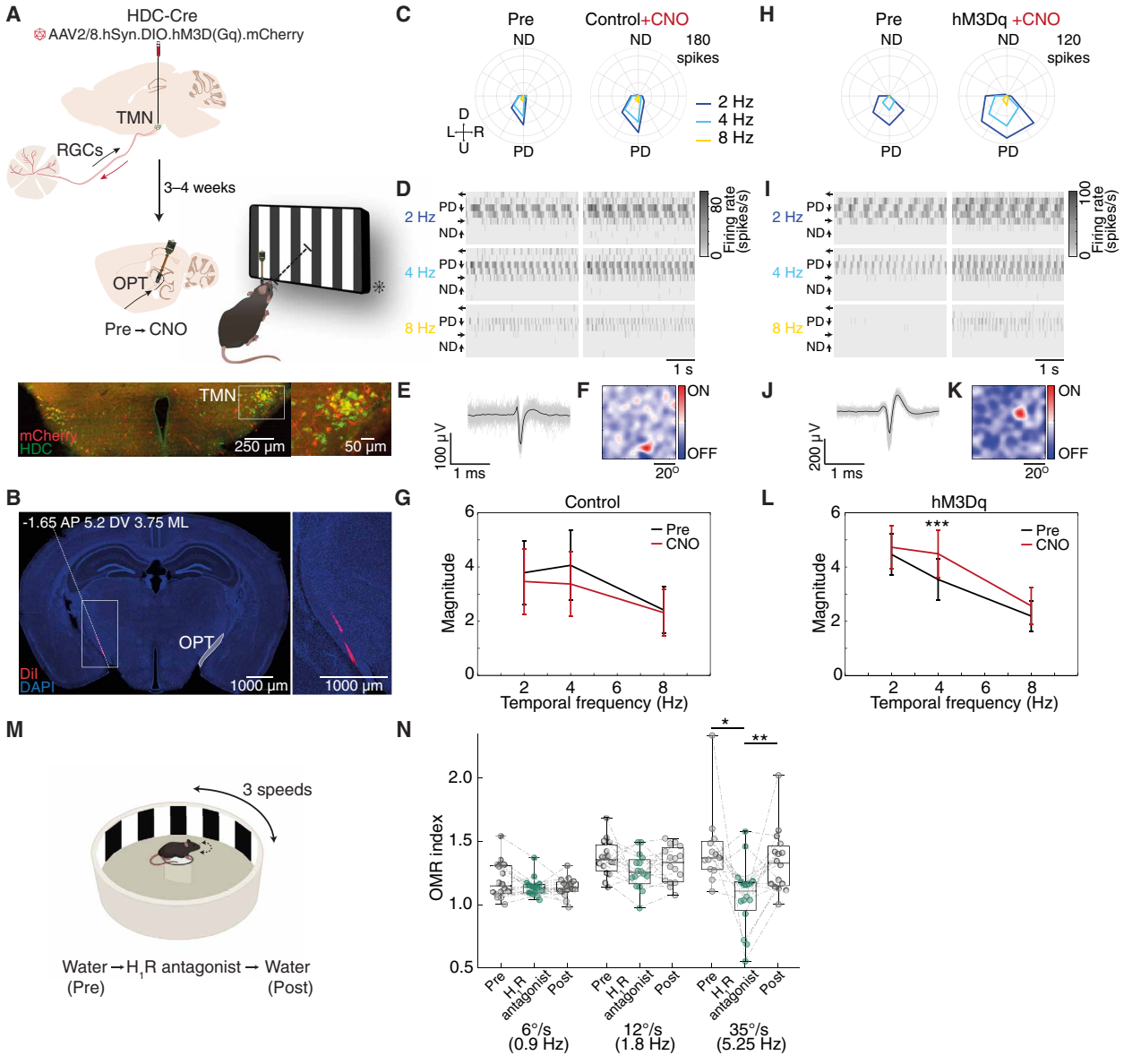

Fig. 5. Activation of histaminergic retinopetal axons enhances DSGCs' responses to higher velocity in vivo. (**A**) Top: Schematic of hM3Dq-mCherry microinjection into the TMN of HDC-Cre mice. Bottom: Neuropixels recordings in the optic tract before and after CNO. Bottom: Immunostaining showing hM3Dq-mCherry$^+$ (red) and HDC$^+$ (green) neurons. (**B**) Left: Tracing of the probe of a recorded mouse. Right: High magnification. (**C**) Polar plots of an example DSGC's axon in a control mouse to moving gratings at different temporal frequencies, before (left) and after (right) CNO. (**D**) Mean firing rates of the cell in (C) to different temporal frequencies denoted on the left, before (left) and after (right) CNO. Notions as in Fig. 4B. (**E**) Mean spike waveform (black) with 100 individual spikes (gray) of the cell in (C). (**F**) Receptive field calculated in response to white noise stimulation of the cell in (C). (**G**) Population data (mean ± SEM) of the first harmonic magnitude of the FFT at the stimulus frequency as a function of temporal frequency for DSGCs axons in control mice ($n = 31$; the effect of CNO is not significant for the two-way repeated-measures ANOVA). (**H** to **K**) Same as in (C) to (F) except for an hM3Dq mouse. (**L**) Same as (G) except for hM3Dq mice ($n = 59$, $P = 0.001$ for 4 Hz). Two-way repeated-measures ANOVA with Bonferroni post hoc correction for multiple comparisons. (**M**) Schematic of the setup for OMR. (**N**) OMR index calculated in response to stimuli moving at 6°, 12°, and 35°/s in C57BL/6J mice ($n = 16$) treated with water (gray) or H_1R antagonist (green). Two-way repeated-measures ANOVA with Tukey's post hoc correction for multiple comparisons. $P = 0.0467$ and $P = 0.0079$ for H_1R antagonist versus Pre and Post. $^*P < 0.05$, $^{**}P < 0.01$, $^{***}P < 0.001$. Abbreviations: OPT, optic tract; D, R, U, and L, down, right, up, and left, respectively; PD, preferred direction; ND, null direction. (A) and (M) adapted from BioRender.com.

to gratings moving at 4 Hz after CNO injection in hM3Dq mice but not in controls (Fig. 5, G and L).

Our data demonstrated that DSGCs show an increased ability to respond to faster-moving stimuli upon activation of histaminergic neurons. Given the established role of DSGCs in the OMR (*48*), a reflex that compensates for shifts in the visual scene, we quantified the effects of histamine on the ability of mice to track globally moving gratings of varying speeds (from 6° to 35°/s, corresponding to 0.9 to 5.25 Hz) (*49*, *50*). Experiments were done in control conditions (water) and 30 min after administering an H_1R antagonist (dimetindene maleate, Fenistil, 10 mg/kg) (Fig. 5M, see Materials and Methods). We found that the OMR index, a measure for the ability

of the mouse to track the moving stimulus (see Materials and Methods), decreased significantly under H_1R antagonist, but only for the highest tested speed (Fig. 5N). Notably, this reduction was reversible, as the OMR returned to normal (Fig. 5N). Together, these in vivo experiments support our ex vivo results (Fig. 4) and demonstrate that histaminergic neurons can modulate retinal output, particularly velocity tuning of DSGCs. Moreover, such modulatory effects may extend to the mouse OMR.

H_1R antagonist nonuniformly affects human's sensitivity across the visual field

Having established a role for histaminergic retinopetal axons in mice, we wondered whether histamine may also affect visual information processing in the human retina, given that retinopetal axons have been found in human retinas (*3*, *51*) and histaminergic retinopetal axons in nonhuman primates (*6*). To study the effect of histamine on human visual sensitivity, we administered the same first-generation H_1R antagonist dimetindene maleate (Fenistil) to eight human volunteers. The participants underwent a series of visual tests twice, once after taking the H_1R antagonist and once after taking a placebo, in a single-blind experimental design (see Materials and Methods). The H_1R antagonist did not affect the participants' levels of concentration, as assessed by total time of the visual tests (table S1).

We first performed a visual field test of the central visual field. Participants were shown spots of light at different intensities at 68 different locations within 10° of the fovea. A visual threshold was then calculated in decibels (dB) for each location (see Materials and Methods). The difference in visual sensitivity between the H_1R antagonist and placebo revealed a slight decrease in nearly all locations (Fig. 6A). Averaging over all locations for each eye revealed a slight but significant decrease in sensitivity with the H_1R antagonist (Fig. 6B). Next, we examined the visual sensitivity in the peripheral visual field (between 30° and 60°; Fig. 6C). The difference in visual sensitivity between the H_1R antagonist and placebo revealed an opposite trend in different locations in the visual field, with the H_1R antagonist causing increased visual sensitivity in the superior field and decreased sensitivity in the inferior field (Fig. 6, C and E). Thus, we calculated the mean visual sensitivity in four locations in the visual field (superior, inferior, nasal, and temporal) and found that the H_1R antagonist significantly increased visual sensitivity in the superior region (Fig. 6D). Our findings suggest that histamine may nonuniformly affect the human retina, decreasing the sensitivity of the ventral retina, which represents the superior visual field, while possibly increasing that of the central retina, which represents the central visual field.

DISCUSSION

Here, we sought to determine how histaminergic retinopetal projections shape retinal processing. We demonstrated that histaminergic projections originating in the TMN of the hypothalamus innervate the retina and can shape the response properties of distinct RGC subtypes. Histamine increases the baseline activity and qualitatively changes the light responses of many RGCs. Specifically, we showed that histamine shortens the light responses of OFF-transient alpha RGCs and improves DSGCs' ability to respond to higher velocity stimuli, a finding that we further validated with in vivo optic tract

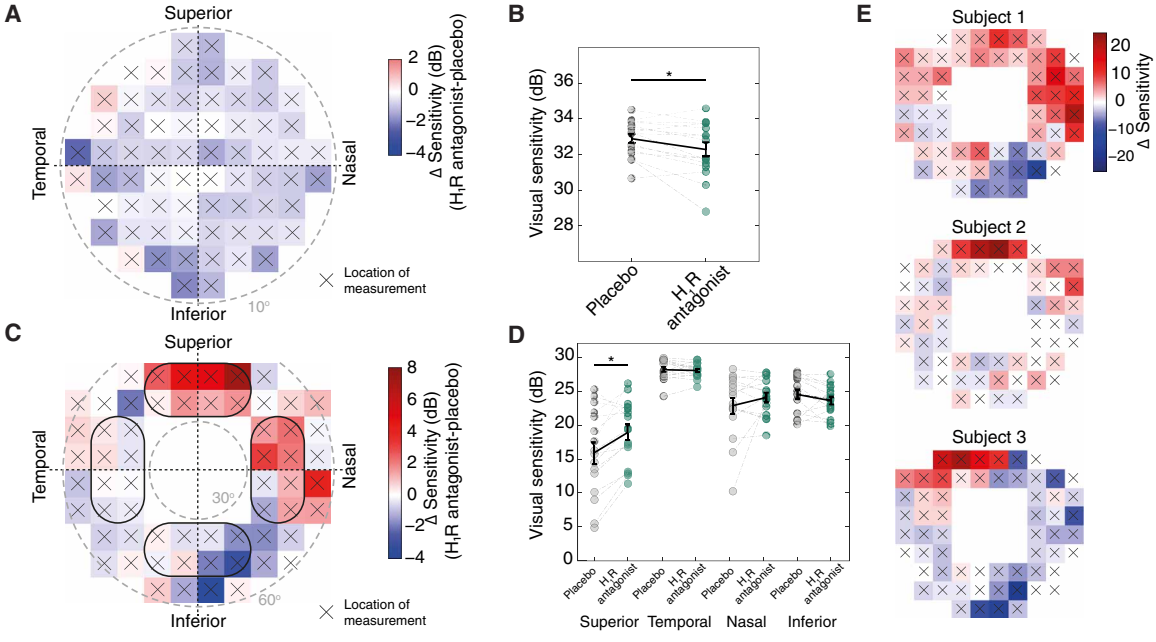

Fig. 6. H_1R antagonist nonuniformly affects visual sensitivity in the peripheral visual field in humans. (**A**) Heatmap showing the mean change in decibels (dB) at each measured location in the central visual field test. The center corresponds to the fovea. Positive (red) and negative (blue) values correspond to increased and decreased sensitivity, respectively, in the presence of the H_1R antagonist compared to the placebo. Gray dashed line labels 10° from the fovea. (**B**) Visual threshold sensitivity with placebo (gray) and with H_1R antagonist (green), calculated by averaging across all locations in the central visual field test. $P = 0.0150$, two-tailed paired *t* test. (**C**) As in (A) for the peripheral visual field test. Gray dashed lines label 30° and 60° of the visual field. (**D**) Visual threshold sensitivity with placebo and H_1R antagonist for each region of the visual field, calculated by averaging across eight locations [outlined in (C)]. $P = 0.0102$, two-tailed paired *t* test with Bonferroni-Holm correction. (**E**) Similar to (C), but for three example participants. $^*P < 0.05$, $n = 16$ eyes from eight participants.

recordings. In addition, we demonstrated that the OMR, a visually guided behavior that requires functional DSGCs (*48*, *50*, *52*), is diminished at high speeds upon the administration of an antihistamine in freely moving mice. Last, we found that administration of the same antihistamine nonuniformly affects humans' visual sensitivity, suggesting that this pathway is evolutionarily conserved across species. Our results reveal a top-down functional circuit of brain-derived histaminergic projections that shape visual processing in the earliest possible site—the retina.

Modulation of visual processing by arousal state

The brain's histaminergic system has long been associated with wakefulness and attention (*26*, *27*, *53*, *54*). Histaminergic neurons are silent during sleep, and their firing rate increases with the arousal state of the animal, peaking during attentive waking (*28*). As our results demonstrate that histamine modulates both the baseline firing and the light responses of RGCs, we can hypothesize that visual processing can change with the arousal state. Neurons in V1, dLGN, and SC were shown to change their baseline and visually driven activity with the level of arousal (*47*, *55*–*63*). The origin of these changes, however, is usually attributed to local neuromodulators, top-down circuits, or local connectivity. Notably, two recent studies revealed that the retinal output itself changes with the mouse's arousal state both in the dLGN (*31*) and in the SC (*30*). Using in vivo two-photon Ca^{2+} imaging of RGCs' axonal boutons, these studies demonstrated that visual responses of almost 50% of them are modulated with locomotion and pupil size, which reflect the arousal state. Typically, these modulations included suppression of visual responses and attenuation of direction and orientation selectivity, although this was only shown for low motion velocity (*30*, *31*).

The arousal-related suppression of visual responses and direction selectivity reported in both the dLGN and SC (*30*, *31*) is in line with our findings that histamine shortens the responses of OFF-transient alpha RGCs and reduces pDSGC responses to spot stimuli and broadens their directional tuning to low velocity motion. Yet, several aspects of the arousal modulation differ between the dLGN and SC. These differences could originate from different subtypes of RGCs that innervate the dLGN and SC (*64*), but they may also have other origins. Other studies have shown that local presynaptic modulation also influences the effects of arousal on the activity of retinal axonal boutons (*65*–*68*). Because RGCs project onto numerous brain targets to transfer the visual information (*69*, *70*), we hypothesize that properties of arousal modulations that serve a specific target would take place locally, while modulations that contribute to all the targets would take place in the retina. For example, when a mouse is aroused and moves through its environment, objects in the visual field have higher apparent velocities. To track these high velocities, we suggest that histaminergic retinopetal axons fine-tune retinal processing during periods of high arousal (e.g., escaping or foraging), shifting the velocity tuning of DSGCs to encode faster motion, a piece of information that otherwise would be lost. Such a shift in DSGCs' velocity tuning may improve OMR performance during high motion speed.

Mechanism of histamine-induced modulation

There are three types of HRs that have been identified in the mammalian retina: H_1R, H_2R, and H_3R and no histamine-forming cells have been identified to date. We identified the H_1R as the primary receptor responsible for the increase in RGCs' baseline activity (Fig. 2), the enhanced responses of posterior preferring DSGCs (pDSGCs) (fig. S8) and OMR to fast-moving stimuli (Fig. 5). These data, combined with our voltage clamp recording in pDSGCs (fig. S6) and the transcriptomic datasets we analyzed (fig. S5), suggest a direct action of histamine on DSGCs via H_1R, bypassing upstream BCs and ACs. To our knowledge, there have been no reports on the expression of H_1R in BCs. However, one study did observe colocalization between H_1R and calretinin in the mouse IPL, leading to the suggestion that the receptor expression may occur on the processes of SACs (*8*). Yet, this result is not in line with the transcriptomic data as there is no evidence of H_1R expression in SACs (fig. S5G), raising the possibility that the immunolabeled H_1R may be present on DSGC processes, which costratify with SACs (fig. S5C, see *Calb1* and *Calb2* mRNA). We hypothesize that the functional changes we observe in DSGCs primarily result from a direct H_1R activation, which leads to an increase in cell excitability (*17*).

Increased excitability may increase the firing rate of DSGCs to various moving stimuli, and in particular enable the cell to fire in response to fast-moving stimuli, which, in control conditions, did not cause the threshold for firing to be met (Fig. 4 and fig. S8). We speculate that the decreased response to static stimuli occurs due to the increased background firing rate, which results in signal-to-noise ratio reduction (Fig. 3). This is less dominant during PD motion as the inhibition and excitation to DSGCs are offset in time (*71*, *72*), resulting in directionally tuned time-locked responses. This result was also confirmed in vivo upon chemogenetic activation of histaminergic retinopetal axons (Fig. 5). It should be noted that CNO has some off-target effects that include inhibition of H_1R binding (*73*, *74*), so it is possible that the changes in RGC activity in the chemogenetic experiments were even underestimated.

Despite the broad expression of H_3R among RGCs indicated by transcriptomic data, only $1.2 \pm 1.3\%$ of all units showed a significant reduction in spiking activity upon histamine application. This may be due to the fact that H_3R expression is not limited to RGCs, but is also broadly expressed in BCs and ACs (fig. S5). Inhibition of inhibitory ACs trough H_3R activation could also result in a relief of inhibition (i.e., disinhibition) in RGCs and BCs, eventually causing RGC excitation. Alternatively, H_3R was reported to have complex isoforms (from nonfunctional to constitutively activated) (*75*, *76*), so its impact on RGCs may be minimal.

Species-specific effects of histamine on retinal cells

Several studies investigated the effects of histamine application on retinal neurons' activity ex vivo. Histamine was found to act on cones and BPs in primates (*21*, *23*) and to enhance the activity of various ACs in mice (*19*, *20*, *23*). Previous reports show that histamine affects >80% of the RGCs, but in a highly variable manner. In primates, histamine either increases or decreases the baseline activity of RGCs, while typically suppressing their light-evoked responses (*24*, *25*). In rats, histamine increases the baseline activity of most affected RGCs, with variable effects on their light-evoked responses (*25*), similar to our findings in the mouse retina. Another study suggested that histamine may act indirectly on RGCs, dissimilar to our observations (*25*). This discrepancy may originate in the different species studied or reflect the fact that RGCs other than DSGCs may also have a presynaptic effect that is non–H_1R-mediated. In both primates and rats, different histamine concentrations (1 to 50 μM) caused similar trends, but effects were stronger with the higher

concentration tested (*25*). Our results similarly show a histamine dose-dependent effect on RGCs activity.

Histaminergic modulation of visual sensitivity in humans

To investigate how an H_1R antagonist may affect human visual sensitivity, we administered dimetindene maleate (Fenistil) orally, which allowed Fenistil to potentially reach not only the retina but also other brain structures innervated by histaminergic axons. This makes it challenging to disentangle the H_1R antagonist' effects on the retina from those on the brain, including drowsiness (*77*). However, several lines of evidence suggest that the effects we observed on visual sensitivity are indeed the result of the H_1R antagonist acting at the level of the retina. First, test time was not increased by the H_1R antagonist, confirming that concentration was not affected by drowsiness. Second, our findings revealed a nonuniform effect in different locations of the visual field: decreased sensitivity in the center of the visual field and increased sensitivity in the superior field. We postulate that if the actions of the H_1R antagonist had occurred downstream to the retina, we may have seen a more uniform effect across the visual field. One possible explanation for the nonuniform effect of H_1R antagonist on the visual field could be due to differential expression of H_1Rs in different areas of the retina. Notably, the flash sensitivity of baboon RGCs recorded ex vivo was shown to decrease with histamine application (*24*), in line with our findings.

While it is not possible to administer histamine to human participants, we hypothesize that this would cause opposing effects, namely, an increase in visual sensitivity in the central field and a decrease in sensitivity in the superior visual field. As the superior visual field has the lowest visual sensitivity to begin with (Fig. 6D), this suggests that humans rely less on the superior visual field and that histamine can tune visual processing to selectively enhance sensitivity in specific areas according to behavioral needs. H_1R antagonists were previously shown to decrease the critical flicker fusion frequency in humans (*78*–*80*), suggesting that histamine also affects temporal sensitivities in the human retina. Because these studies, as well as ours, only tested a selective H_1R antagonist, while all three HRs are expressed in the primate and human retina (*19*, *21*, *81*, *82*), histamine's effects on retinal processing may be even more complex.

Neuromodulators in the visual system

Over the years, the search for mammalian retinopetal axons, and particularly their origin, has led to opposing findings even within species. Studies based on axonal tracers reported various origins, including the hypothalamus, various visual structures, the oculomotor nucleus, and the dorsal raphe nucleus (*83*–*89*). Other studies failed to label any brain area or interpreted somatic labeling in the brain as the result of transneuronal transport (*90*–*93*). In most of these investigations, the axonal tracers labeled only a few cell bodies, which contributed to the difficulty of finding the retinopetal axons and their origin. Here, we took advantage of the HDC-Cre mouse lines to indisputably identify histaminergic neurons in the TMN as a source for retinopetal axons. Future work may make use of other transgenic mouse lines to resolve whether other brain regions also contribute to visual processing in the retina. In particular, it was suggested that serotonergic neurons in the dorsal raphe nucleus send projections to the retina (*94*–*96*). If true, this suggests that the histaminergic and serotonergic systems, which contribute to higher cognitive functions, including wakefulness and mood, may interact already at the level of a primary sensory organ.

MATERIALS AND METHODS

Experimental design

This study explores how a subset of histaminergic neurons of the TMN projects to the retina and modulates retinal visual processing. Initially, we verified their presence through Cre-dependent anterograde tracing in HDC-Cre mouse lines. Subsequently, we examined the impact of histamine application and its receptor blockers on RGCs' activity ex vivo, both under baseline conditions and during visual stimulation. For this, we used several approaches, including MEA recordings, two-photon Ca^{2+} imaging, and targeted patch-clamp experiments, focusing particularly on direction-selective RGCs (DSGCs). We investigated the expression of HRs in different retinal cell types to correlate our physiological findings and observed a higher expression level in DSGCs. We then conducted in vivo Neuropixels recordings of RGC axons in the optic tract of anesthetized mice, coupled with chemogenetic activation of HDC neurons, to investigate the brain's contribution to DSGCs' output while animals were exposed to grating stimuli moving at various speeds. After this, behavioral experiments involving freely moving mice exposed to stimuli moving at different speeds were conducted while blocking HRs, allowing us to assess the effects of inhibiting this circuit. Last, we used the same drug to study its effects on human participants.

Mice models and ethics statement

Two-photon targeted recordings from pDSGCs were performed using Trhr-EGFP mice (MMRRC, strain no. 030036-UCD), which express GFP in posterior-preferring ON-OFF DSGCs (*97*). Two-photon Ca^{2+} imaging and two-photon targeted recordings from alpha-RGCs were conducted from the GCL of the isolated retina of mice expressing GCaMP6f in RGCs (the Jackson Laboratory, strain no. 025393) (*98*). Intracranial injections were performed on C57BL/6J mice (purchased from Charles River Breeding Laboratories) and on two HDC-Cre mouse lines, which express Cre recombinase under the control of the *hdc* promoter [the Jackson Laboratory, strain no. 021198 (*99*) and MMRRC, strain no. 037409 (*100*, *101*)]. MEA experiments were performed on wild-type mice from the same colony. Weaned mice from either sex, 4 to 12 weeks old, were housed in groups of no more than five in individual cages at 25°C in a 12-hour/12-hour light-dark cycle with water and food provided ad libitum. All procedures were approved by the Institutional Animal Care and Use Committee at the Weizmann Institute of Science (nos. 08161123, 04560522, 07000820, 04920522, and 15530719).

Intracranial AAV injections

To label retinopetal axons in C57BL/6J mice, 0.5 to 1 μl of AAV2/8.hSyn.mCherry (HUJI Vector Core no. 7.19) or AAV2/8.hSyn.Chronos.tdTomato (Addgene no. 62726) was injected into the TMN based on stereotactic coordinates (injection site: anteroposterior = −2.6 mm; mediolateral = 0.7 mm; dorsoventral = −5.3 mm from bregma). To label histaminergic retinopetal axons in HDC-Cre mice, we used Cre-dependent adeno-associated viruses (AAV2/1.CAG.Flex.tdTomato.WPRE.SV40 or AAV2/8.CAG.Flex.tdTomato.WPRE.SV40, Harvard Vector Core, lot nos. 704 and 605, respectively). For chemogenetic electrophysiological experiments, mice were bilaterally injected in the TMN with AAV2/8.hSyn.DIO.hM3D(Gq)-mCherry (HUJI Vector Core no. 35.18).

For the injection procedure, mice were anesthetized with inhalant isoflurane (5% induction and 1.5 to 2% maintenance, SomnoSuite,

Kent Scientific) and administered with 0.5 ml of saline via intraperitoneal injection, to avoid dehydration. The animal was kept on a closed loop heating pad and watched for vitals throughout the surgery and its eyes were kept from drying with a layer of Synthomycine (ABIC Ltd., TEVA Pharmaceutical Industries Ltd., Israel). Next, a craniotomy of 1 to 2 mm was made, 2.5 to 2.8 mm posterior and 0.7 to 1 mm mediolateral to bregma. A Hamilton syringe (1 μl, 65458-01) was then lowered into the brain at a rate of 10 μm/s to target the TMN. The viral solution was delivered at 0.1 μl/min after a 10-min pause to allow the brain to resettle. The scalp incision was sealed with a tissue adhesive (Histoacryl, Melsungen AG, Germany) and mice were left to recover post-surgery, after subcutaneous injections of antiseptic analgesia (0.01xNorocarp, Norbrook Laboratories Limited, Newry Co. Down, Northern Ireland, 10 μl/gr).

Tissue processing, immunohistochemistry protocols, and microscopy

Immunohistochemical analysis of virus expression (reporter gene, mCherry or tdTomato) in combination with the identification of histaminergic neurons via HDC immunohistochemistry was performed on mouse brain slices 3 to 4 weeks after the injection (primary antibody: rabbit polyclonal anti-HDC, 1:300, PROGEN Biotechnik GmbH, cat. no. 16045; secondary antibody: donkey anti-rabbit 488, 1:200, Invitrogen A21206). Mice were deeply anesthetized with a terminal intraperitoneal injection of pentobarbital (pentobarbital sodium, 200 mg/ml, CTS Chemical Industries Ltd., Kiryat Malachi, Israel), then intracardially perfused with phosphate-buffered saline (PBS, Biological Industries Israel, 02-023-1A, pH 7.4) and 4% paraformaldehyde (PFA, ChemCruz, Santa Cruz Biotechnology Inc., CAS: 30525-89-4) before brain and eye extraction. Eyecups were fixed for 1 hour (4% PFA) and then hemisected to obtain whole mount retinas.

Brains were fixed further for 24 to 48 hours in 4% PFA and washed in PBS, then sliced (30 μm) by a vibratome (7000 smz-2 Vibratome, Campden Instruments Ltd.). Slices were washed three times in PBS and subsequently blocked with 0.25% PBST (PBS + Triton X-100, Sigma-Aldrich, CAS: 9002-93-1) with 3% bovine serum albumin (BSA, MP Biomedicals, cat no. 160069) for 2 hours at room temperature, followed by overnight immersion in primary antibody solution (1% BSA and 0.1% Triton X-100 in PBS with antibody-specific dilution) at 4°C on a shaker. The next day, slices were washed in PBS and immersed in a secondary antibody solution overnight (1% BSA in PBS with antibody-specific dilution). Slices were mounted onto Superfrost/Plus Microscope Slides (Thermo Fisher Scientific), covered with a coverslip using Vectashield antifade mounting medium with DAPI (4′,6-diamidino-2-phenylindole) (Vector Laboratories, H1200). All brain sections were digitally scanned using Olympus UPlanSApo 10×/0.40 NA (numerical aperture) or 20×/0.75 NA objectives on an Olympus BX61VS slide scanner (Olympus Corporation, Tokyo, Japan).

Retinal whole mounts were blocked with 0.25 to 0.4% PBST with 3 to 5% BSA for 2 hours at room temperature and then incubated for 2 days in primary antibody solution (1% BSA and 0.1% Triton X-100 in PBS; primary antibodies: goat polyclonal anti-RFP antibody, 1:300, MyBioSource, cat. no. M5448122) at 4°C on a shaker. The next day, retinas were washed in PBS and overnight immersed in a secondary antibody solution (1% BSA in PBS with antibody specific dilution; secondary antibodies: donkey anti-goat 568, 1:1000, Invitrogen, cat. no. A11057). The tissues were stained with DAPI to identify nuclei and mounted onto Superfrost/Plus Microscope Slides, covered with a coverslip, using a Vectashield antifade mounting medium with DAPI. Retinal whole mounts were imaged using an inverted laser scanning confocal microscope (Zeiss, Oberkochen, Germany) equipped with 488-, 543-, and 633-nm laser lines, using ZEN software (Zeiss). Optic nerves were directly mounted and covered with a coverslip. Tiled images of the whole retina and optic nerves were acquired using a 20×/1.0 W Plan Apochromat DIC VIS-IR 75-mm objective. Further image processing for brain slices and whole mount retinas and optic nerves was performed with Fiji and QuPath software (*102*, *103*).

Image analysis

To assess the accuracy of histaminergic neurons (HDC^+) genetic labeling, virally injected HDC-Cre mice (MMRRC strain no. 03740) brains were visualized using QuPath, and the 14 ± 1.4 slices closest to the injection site in the TMN were further analyzed. For quantification, HDC^+ were first detected and counted using the manual counting tool. Reporter gene positive cells ($tdTomato^+$) were then annotated in two different classes as $tdTomato^+/HDC^+$ or $tdTomato^+/HDC^-$ according to their immunoreactivity for HDC. The number of points and their coordinates have been saved. The percentage of HDC^+ cells that were $tdTomato^+$ (efficiency) and total $tdTomato^+$ (both HDC^+ and HDC^-) that were HDC^+ (specificity) were calculated for each slice and averaged for each brain.

To compare the Cre recombinase activity of the two HDC-Cre mouse lines (the Jackson Laboratory, strain no. 021198 and MMRRC strain no. 03740), we crossed them with an Ai9 Cre reporter mouse line (the Jackson Laboratory, strain no. 007909) that expresses tdTomato after Cre recombination. Efficiency and specificity were quantified as above. Our analysis revealed an average efficiency of 89.9% and specificity of 52.3% ($n = 2$ mice) in the TMN of HDC-Cre Jackson X Ai9 mice, whereas the HDC-Cre MMRRC X Ai9 mice had an average efficiency of 48.7% and a specificity of 75.6% ($n = 2$ mice).

Tissue preparation for physiology

Mice were kept in dark-adapted conditions for at least 30 min and then anesthetized with isoflurane (Terrell, Piramal Critical Care Inc.) and decapitated. Eyes were immediately enucleated and dissected under dim red and infrared light in a petri dish containing Ames solution (Sigma-Aldrich, St. Louis, MO, USA) supplemented with 1.9 g/liter of sodium bicarbonate saturated with carboxygen (95% O_2 and 5% CO_2). The orientation of the retina was determined based on landmarks on the choroid as described previously (*104*), and retinas were dissected in two halves along the nasal-temporal axis. Retinas were kept in the dark at room temperature in Ames solution bubbled with carboxygen until used.

For MEA recordings, MEAs were precoated with poly-D-lysine solution (PDL, 1.0 mg/ml in H_2O, Merck-Millipore, CAT: A-003-E) for 1 hour at room temperature. After washing off the PDL, one-half of the retina was mounted on the MEA with the RGC layer facing the electrodes, as previously described in (*105*). For targeted patch-clamp recordings, retinas were cut into half, isolated from the pigment epithelium, and mounted, photoreceptor side down, over a hole of 1 to 1.5 mm^2 on a filter paper (GSWP01300, Merck Millipore, Billerica, MA, USA). For two-photon Ca^{2+} imaging, retinal pieces were mounted onto poly-D-lysine–coated 12-mm coverslips (product number 354086, Corning, Glendale, AZ, USA).

Histamine application and pharmacology

Histamine (Sigma-Aldrich, product number H7250) containing Ames solution was prepared fresh from powder for each experiment (5 to 20 μM). HR blockers, cetirizine dihydrochloride (H_1R; Tocris, Bristol, UK, product number 2577), and JNJ 5207852 (H_3R; Tocris, product number: 4020) were dissolved in water to make stock solutions of 20 mM and then were further diluted in Ames solution to a working concentration of 20 μM. HR blocker famotidine (H_2R; Sigma-Aldrich, St. Louis, MO, USA, product number: F6889) was dissolved in dimethyl sulfoxide (DMSO) to make a stock solution of 80 mM and then was further diluted in Ames solution to a working concentration of 40 μM.

Targeted patch-clamp recordings

Retinas were placed under a two-photon microscope (Bruker, Billerica, MA, USA) equipped with a Mai-Tai laser (Spectra-physics, Santa Clara, CA USA) and perfused with oxygenated Ames solution at 32 to 34°C. Identification of and recording from GFP^+ RGCs were carried out as previously described (*97*, *104*). In short, GFP^+ cells were identified using the two-photon microscope laser at 920 nm, to avoid bleaching of the photoreceptors. pDSGCs were targeted in Trhr-EGFP mice retinas. Alpha RGCs were targeted by finding RGCs whose cell bodies had a diameter greater than 20 μm (*41*). The inner limiting membrane above the targeted cell was dissected under the microscope with a glass electrode using infrared illumination. Loose-patch recordings (holding voltage set to "OFF") were performed with a clean glass electrode (3 to 5 megohms) filled with Ames solution. Every alpha RGC was recorded in both conditions, i.e., control and histamine. For the spot stimuli, some pDSGCs were recorded only under one condition, control or histamine application. For velocity tuning, all pDSGCs were recorded in both conditions (before and after histamine). We did not present the faster stimuli (8 or 10 Hz) for two cells that stopped responding at intermediate temporal frequencies. For all other cells, we presented all temporal frequencies regardless of the responses.

Intracellular voltage-clamp recordings from pDGSCs were carried out using glass pipettes (5 to 9 megohms) filled with an intracellular solution containing 110 mM $CsMeSO_4$, 2.8 mM NaCl, 4 mM EGTA, 20 mM Hepes, 5 mM TEA-Cl, 4 mM Mg-ATP, 0.3 mM Na_3GTP, 10 mM Na_2-phosphocreatine, and 5 mM *N*-ethyllidocaine chloride (QX314), pH 7.25, osmolarity = 290, $E_{Cl} = -73$ mV. A gigohm seal was obtained before breaking in. Data were acquired at 20 kHz and filtered at 2 kHz, with a Multiclamp 700B amplifier (Molecular Devices, CA, USA) using pCLAMP 10 recording software and a Digidata 1550 digitizer (Molecular Devices). The evoked EPSCs in pDSGCs were isolated by holding the cells at −60 mV. Liquid junction potential was corrected. All cells ($n = 9$) were recorded before (Control) and after histamine application (Histamine).

Visual stimuli used in patch-clamp experiments

Stimuli were generated using MATLAB and the Psychophysics Toolbox (*106*, *107*). A white, monochromatic organic light-emitting display (OLED-XL, 800 pixel × 600 pixel resolution, 85 Hz refresh rate, eMagin, Bellevue, WA, USA) was used. The display image was projected through a 20× water-immersion objective (UMPLFLN20xW; Olympus, Tokyo, Japan), via the side port of the microscope, centered on the soma of the recorded cell, and focused on the photoreceptor layer. The diameter of the entire display on the retina was 1 mm across. The light intensity of the gray screen was 6.4×10^4 R^*rod^{-1} s^{-1}. For the spot stimulus, a gray background was presented for 2 s, followed by the appearance of a black (for OFF alpha RGCs) or white (for ON alpha RGCs and pDSGCs) spot on the gray background for 2 s, followed by a return to the same gray background for a further 2 s. Spots of different diameters (50 to 800 μm) were presented in a pseudorandom order. The total number of spikes was averaged over five repeats. The grating stimulus consisted of moving square-wave gratings with a spatial frequency of 400 μm. For testing different motion velocities, we used temporal frequencies ranging from 1 to 10 Hz, corresponding to 400 to 4000 μm/s. The grating stimuli were presented in eight different pseudorandomly chosen directions, in 45° intervals, with each presentation lasting 3 s, followed by 2.5 s of a gray screen. The stimulus was masked by a circle (diameter 400 μm) so that everything outside the circle remained gray. The total number of spikes was averaged over three to four repeats. For the moving-bar stimuli, a white bar (400 μm width × 900 μm length) on black background moved through the center of the screen in eight different pseudorandomly chosen directions, in 45° intervals, at a speed of 600 μm/s. Each presentation was separated by 2 s of mean gray screen. The total number of spikes was averaged over 4 repeats.

Data analysis of patch-clamp experiments

Electrophysiological data were analyzed offline. For loose-patch clamp recordings, spike times were extracted after filtration using a 4-pole Butterworth band-pass filter between 80 and 2000 Hz. Peristimulus time histograms (PSTHs) of spiking activity were calculated from five repeats using a bin width of 50 ms for spot stimuli. For moving grating stimuli, mean PSTHs were calculated using a 25-ms bin width. For spot stimuli, the background activity was determined based on the 2-s period of initial gray screen in each trial. This provided the mean background activity and its SD. The bin with the highest firing rate during the spot appearance (or disappearance in the case of OFF responses in pDSGCs) was used to calculate the maximum response. Response durations were defined based on the number of all the bins during the stimulus whose value exceeded the mean background activity by 3 SDs (*35*). Statistical tests to compare response durations were performed on log-transformed ($\log_{10}$) values of the duration, which were then distributed normally. To analyze responses to moving gratings, we calculated the normalized vector sum (or global DSI) as $gDSI = \frac{|\Sigma R_\theta e^{i\theta}|}{\Sigma R_\theta}$, where R_θ is the response in direction θ, defined as the mean number of spikes during the grating presentation (averaged over repetitions). To analyze temporal tuning, we set the gDSI to 0 for cells that stopped responding (<2 spikes/s in response to gratings). We determined the PD as the direction that most frequently had the maximum response across both conditions (pre and histamine) and temporal frequencies (1 to 6 Hz). The normalized response in the PD was calculated as the total number of spikes in the PD divided by the maximum number of spikes from any temporal frequency or condition (pre and histamine). Of 11 targeted pDSGCs GFP^+ cells, 10 had a gDSI >0.15 in the pre–2-Hz condition and 9 of 11 recorded Trhr GFP^+ cells had a DSI > 0.3 in the pre–2-Hz condition (see also the "Analysis of MEA light responses" section for the definition of DSGCs). Excluding cells with gDSI and DSI below thresholds did not affect population analysis. Statistical comparison was performed with a two-way analysis of variance (ANOVA) with Bonferroni post hoc correction for multiple comparisons.

In voltage-clamp intracellular recordings, spontaneous miniature EPSCs (mEPSC) were detected as fast high-frequency events that are more than 3 SD above baseline current. The baseline current

was calculated from the filtered current using Savitzky-Golay filtration (order of 1, 1301 frame length) across 50 s before and after histamine application, respectively. Consequently, the frequency of the mEPSCs was calculated as the number of detected events per second in each condition (mEPSC/s). mEPSC amplitude was defined as the difference between the maximum value of each detected event and the baseline current. Cells that had baseline current lower than 100 pA when breaking in were removed from the analysis.

Two-photon Ca^{2+} imaging

Two-photon Ca^{2+} imaging (Bruker microscope equipped with a Spectra-Physics Mai-Tai laser) from the GCL of the isolated retina of mice expressing GCaMP6f in RGCs (Thy1-GCaMP6f) was carried out on an area of 140×140 μm^2 at 6 Hz. For the UV stimuli, a modified projector (M109s DELL, Austin, TX, USA) containing a UV LED (NC4U134A, peak wavelength 385 nm; Nichia, Anan, Japan) was used (*108*). The image was projected onto the retina via the microscope's condenser and created on the photoreceptor layer using two converging lenses (LA4372 and LA4052; Thorlabs). The field of view was positioned in the center of the visual stimulus. Control experiments, in which histamine was not added, were performed using the same time course as the histamine experiments. Histamine was added 10 min before imaging under histamine conditions. Histamine was washed out with Ames solution for 45 min before imaging.

For UV spot stimuli, a spot (300 μm in diameter) of increased luminance (2.8×10^4 R*rod^{-1} s^{-1}) centered on the field of view (140×140 μm^2) appeared for 2 s. The $\Delta F/F$ was averaged over 3 trials.

Data analysis of two-photon Ca^{2+} imaging experiments

Regions of interest were manually selected using an average projection of the responses to the stimulus (all repeats) with ImageJ software (*109*). Each field of view contained between 9 and 38 RGCs. To determine whether an RGC responded to the histamine application, the mean baseline and SD were calculated from the 30 s immediately before histamine arriving in the bath. RGCs whose responses exceeded 6 SDs over the mean baseline in the 40-s period after histamine's arrival were counted as responsive to histamine. Before any visual stimulus, the RGC layer was imaged for 30 s. The latter 15 s of this prestimulus were taken as the baseline and used to calculate the $\Delta F/F$. To determine whether an RGC was responsive to a spot stimulus, a threshold of 3 SDs above the mean baseline was set during the ON period (appearance of white spot) and OFF period (2 s after the spot disappeared). An additional threshold was set 3 SDs below the mean baseline during the ON period. Any RGC whose $\Delta F/F$ trace crossed any of these thresholds was counted as light responsive. To determine whether an RGC response polarity was ON or OFF, we used an ON-OFF index (OOI): $\mathrm{OOI} = \frac{R_{ON} - R_{OFF}}{R_{ON} + R_{OFF}}$, where R is the maximum amplitude ($\Delta F/F$). RGCs with a negative OOI were deemed OFF RGCs, whereas those with a positive OOI were deemed ON RGCs. As the responses of some RGCs changed with time, only RGCs that had the same response polarity (ON, OFF, or nonresponsive) under the pre- and histamine-washout conditions were included [54% (276 of 512) for histamine dataset; 70% (98 of 140) for control dataset]. In the statistical analysis using Fisher's exact test, all changing RGCs were grouped together and all nonchanging RGCs were grouped. RGCs were classified as changing if they lost, gained, or changed response polarity. Response amplitudes before and after histamine were calculated in units of SDs (based on the 15-s baseline recording) and were plotted against each other, and the absolute distance from the unity line was calculated and their distribution were compared using a Kolmogorov-Smirnov test. In fig. S4 (C to H), RGCs were further divided into transient and sustained groups. For OFF RGCs, this was done by calculating a transient-sustained index where the mean of the response trace (during the OFF period) was divided by the maximum amplitude (during the OFF period). Those RGCs with a transient-sustained index >0.4 were deemed sustained, whereas those <0.4 were considered transient. For ON RGCs, the transient-sustained index was calculated in the same way, except for using the ON period and a further step where, if the maximum amplitude occurred during the first half of the ON period, the transient-sustained index was further divided by 2. Those RGCs with a transient-sustained index >0.35 were deemed sustained, whereas those <0.35 were considered transient.

MEA recordings

MEA recordings were performed on isolated retina using MEAs of 252 electrodes (MultiChannel Systems, 252 electrodes, 30 μm diameter, 100 μm minimal electrode distance). The retina was mounted on the MEA with the GCL facing down. The MEA was placed in the head stage with constant perfusion of oxygenated bicarbonate-buffered Ames solution at a flow rate of 3.5 ml/min; a heating pad placed below the array maintained the temperature at 33.2°C. Data acquisition started 1 hour after the retina was placed in the chamber, to let the retina adapt. Extracellular voltage signals were amplified and digitized at 20 kHz and saved for offline analysis.

Visual stimuli were created in MATLAB (version R2018a), using Psychophysics Toolbox (*106*, *107*) and a custom graphical user interface, and were projected via a monochromatic white OLED display (eMagin, EMA-100309-01 SVGA+, 600 × 800 pixels, 60 Hz refresh rate) through a telecentric lens (Edmund Optics, 2.0X, no. 58-431) onto the photoreceptors. The pixel size on the retina was 7.5 μm. At maximum brightness, the irradiance used in the experiments was 2.6 μW/cm^2, resulting in 2.43×10^4 mouse rod isomerizations (R*rod^{-1} s^{-1}), whereas the minimum brightness was 7.04×10^1 R*rod^{-1} s^{-1}.

Visual stimuli for MEA recordings

We used a battery of visual stimuli in the MEA recordings. All stimuli were presented in full-field, covering the entire electrode array (electrode area: 1500×1500 μm^2, stimulus size was always at least 2250 μm in diameter). We recorded 30 s of spontaneous baseline activity before presenting each stimulus. Stimuli were repeated five times unless otherwise specified. The full-field stimulus sequence was 3 s black, 2 s white, and 3 s black, and the full screen was illuminated in uniform intensity. To test direction selectivity, we used moving square-wave gratings of 100% contrast with a spatial frequency of 397.5 μm (0.075 cycle/°) and various temporal frequencies: 1, 2, 4, 6, 8, and 10 Hz. The gratings moved in eight directions, in 45° intervals, in a randomized order (3 s grating, four repeats, each trial preceded and followed by 2 s of mean gray background intensity).

Histamine concentration calibration

To obtain a dose-response curve for different concentrations of histamine, we performed MEA experiments in which we successively washed in 1, 2, 5, 10, and 20 μM histamine to the bath solution while recording the baseline activity of RGCs in darkness (OLED switched off). Each concentration was washed for approximately 2 min before switching to the next concentration. We recorded a

transistor-transistor logic (TTL) pulse whenever we switched to the next concentration. Control experiments were performed in the same way without washing in any histamine. The time points t_1 to t_5 in the control experiments, shown in fig. S2, correspond to histamine concentrations 1, 2, 5, 10, and 20 μM, respectively. Given that we observed a plateau between 5 and 20 μM both in the magnitude of the response and proportion of RGCs that react to histamine, we used drug concentrations within this range.

Data analysis of MEA experiments

Spike sorting was performed using Kilosort2.0 (*110*, *111*), with subsequent manual curation in Phy (*112*, *113*). We only included well-separated units in our analysis, as determined by refractory period violations (RPVs) <1% (*114*). Data were analyzed using custom-written scripts in MATLAB (version R2018b and R2019b).

Histamine concentration calibration analysis

To analyze the concentration-dependent effect of histamine, spike times were binned using time bins of 1 s. We calculated the mean firing rate over a window of 30 s just before the switch to the next concentration occurred (gray shaded bars in fig. S2A). We then calculated the difference between each mean firing rate to the baseline (0 μM histamine or t_0 in control experiments; fig. S2, C and D). The percentage of responsive RGCs for each concentration (fig. S2E) was determined as described later (see the "Histamine wash-in analysis" section). In total, 112 RGCs with a minimum firing rate of 1 Hz across the duration of the wash-in from three retinas were used in the histamine calibration experiments, and 302 RGCs from four retinas were used in the control experiments.

Histamine wash-in analysis

To analyze the effects of histamine on the baseline activity of RGCs recorded using the MEA, we calculated the firing rate over the duration of the wash-in (15 to 20 min) using a bin width of 1 s. We focused on the time window of 4 min duration after histamine reached the bath and compared the mean firing rate of RGCs to their baseline firing rate (calculated from a 60-s time window in Ames solution just before histamine was added). We only included RGCs with a minimum firing rate of 1 Hz across the duration of the wash-in ($n = 822$ of 1010 from eight retinas for control, and 681 of 742 RGCs from seven experiments for histamine). The magnitude of change in baseline activity was calculated as the difference in firing rate from that of the baseline. We defined cells as responsive to histamine if they crossed an upper or lower threshold, determined by the upper and lower 2.5% quantile of the control distribution (3.6 and −3.8 spikes/s, respectively; Fig. 2B, red vertical lines). We used the same thresholds to determine the percentage of responsive RGCs in the concentration calibration experiments (fig. S2E). The percentage of RGCs with increased firing rates upon histamine application was compared to the control dataset using a two-sample t test for unequal variances.

Analysis of MEA light responses

To classify RGCs as ON, OFF, or ON-OFF, we defined an OOI, calculated from the response to the full-field stimulus: $\mathrm{OOI} = \frac{R_{ON} - R_{OFF}}{R_{ON} + R_{OFF}}$, where R_{ON} and R_{OFF} are the spike counts during 2 s of light ON or OFF, respectively. This results in values in the range of [−1, 1], where ON RGCs will have a positive OOI, OFF RGCs will have a negative OOI, and ON-OFF RGCs will have OOIs in between, depending on whether their ON or OFF response is more prominent. The PSTH in response to the spot stimulus (Fig. 2C) was calculated as the mean PSTH over five repetitions using a bin width of 50 ms. To identify DSGCs, we analyzed the response to moving gratings. Before analysis, motion directions were aligned to retinal coordinates. We then calculated the gDSI as above (see the "Data analysis of patch-clamp experiments" section). The PD was defined as the angle of the vector sum. The direction-selectivity index (DSI) was calculated as $\mathrm{DSI} = \frac{R_{PD} - R_{ND}}{R_{PD} + R_{ND}}$, where R_{PD} and R_{ND} are the responses in the direction closest to the PD and the one opposite to it, respectively. Similarly, we calculated an orientation-selectivity index as $\mathrm{OSI} = \frac{(R_{PD} + R_{ND}) - (R_{OD1} + R_{OD2})}{(R_{PD} + R_{ND}) + (R_{OD1} + R_{OD2})}$, where R_{PD} and R_{ND} make up the response in the preferred axis, and R_{OD1} and R_{OD2} are the responses in both orthogonal directions. We only considered RGCs that had a mean firing rate >1 Hz during the grating stimulus. Cells with a gDSI > 0.15, a DSI > 0.3, and OSI < 0.3 were considered as DSGCs.

To analyze responses of DSGCs to moving gratings of different temporal frequencies, we classified RGCs as DSGCs based on their response to 2-Hz moving gratings, using the same criteria as before. We obtained 27 of 385 DSGCs (three retinas, minimum firing rate of 1 Hz during the moving gratings stimulus). We defined the PD as the direction closest to the angle of the gDSI for gratings moving at 2 Hz. We then performed an FFT on the PSTHs of each DSGC's PD (mean PSTH over four repetitions, using a 25-ms bin width, with mean subtracted) for all temporal frequencies presented and calculated the amplitude of the first harmonic at each stimulus frequency. Statistical comparison was performed with a two-way ANOVA with Bonferroni post hoc correction for multiple comparisons.

In vivo Neuropixels recordings

For the in vivo Neuropixels recordings, we used HDC-Cre mice from the Jackson Laboratory (strain no. 021198; see the "Image analysis" section above). Before electrophysiological recording, mice underwent surgery under isoflurane anesthesia [5% induction and 1.5 to 2.5% maintenance, SomnoSuite (Kent Scientific)] to implant head bars. A craniotomy was then prepared to access the optic tract (opt). Briefly, mice were sedated with an intraperitoneal injection of chlorprothixene (Sigma-Aldrich), then anesthetized with urethane (intraperitoneal, Sigma-Aldrich) and kept on a feedback-controlled heating pad at 37°C. After securing the mouse on a stereotactic device (Scientifica), the scalp was removed to expose the skull. A thin layer of paraffin-based transparent ophthalmic ointment was applied (Duratears, Alcon) to prevent the eyes from drying. After horizontal alignment of the pitch and roll head axes, a craniotomy of 1 to 2 mm in diameter was drilled and the exposed brain was covered with a layer of saline throughout the recording.

Electrophysiological recordings were made with Neuropixels probes (*115*) in head-fixed mice. A Neuropixels probe ("Neuropixels 1.0") was secured to a three-axis micromanipulator (Luigs & Neumann). The probe's tip was dipped into a 1-μl droplet of CM-DiI before insertion to track the probe during the imaging step. The probe was slowly inserted into the brain through the craniotomy, and after reaching the desired depth, it was allowed to settle before starting the recording session. A black curtain was lowered over the rig, keeping the mice in complete darkness except for the visual stimulus. The same visual stimuli (see the "Visual stimuli used in Neuropixels experiments" section) were repeated before and after CNO (clozapine-N-oxide dihydrochloride, Tocris, cat. no. 6329) injection (3 μg CNO/g of mouse body weight) in both control (noninjected HDC-Cre mice) and hM3Dq-AAV-injected mice.

Neuropixels data were acquired at 30 kHz (spike band) using the SpikeGLX recording system (SpikeGLX, https://billkarsh.github.io/SpikeGLX). Kilosort2 was used offline to identify spike times and assign spikes to individual units (*59*, *111*), with subsequent manual curation in Phy (*112*, *113*). After the recording session, probes were retracted from the brain. Mice were deeply anesthetized with a terminal intraperitoneal injection of pentobarbital (pentobarbital sodium, 200 mg/ml, CTS Chemical Industries Ltd., Kiryat Malachi, Israel), and intracardially perfused as described in the "Tissue processing, immunohistochemistry protocols, and microscopy" section. Brains were sliced (30 μm) by a vibratome (7000 smz-2 Vibratome, Campden Instruments Ltd.) and mounted onto Superfrost/Plus Microscope Slides (Thermo Fisher Scientific), covered with a coverslip using a Vectashield antifade mounting medium with DAPI (Vector Laboratories, H1200). All brain sections were digitally scanned using Olympus UPlanSApo 10×/0.40 NA objectives on an Olympus BX61VS slide scanner (Olympus Corporation, Tokyo, Japan). Reconstruction of the fluorescent probe track was obtained in coronal slices using the SHARP-Track tool (https://github.com/cortex-lab/allenCCF) from (*116*) and each point along the probe was translated into the Allen Institute Common Coordinate Framework (CCFv3) template brain. Each CCFv3 coordinate corresponds to a unique brain region, identified by its structure acronym (e.g., CA3, TH, fp, etc.). Only units recorded in the opt (Optic tract) were used for further analysis.

Visual stimuli used in Neuropixels experiments

Visual stimuli were generated using MATLAB custom scripts based on the Psychophysics Toolbox and displayed using an LG LCD gamma-corrected monitor (1280 × 720 pixels, 60 Hz refresh rate), which was positioned 25 cm from the mouse and spanned 137.6° × 77.4° of its visual field (because 1° in the visual field covers 30 μm on the mouse retina, the calculated pixel-to-degree ratio is approximately 9.3). Experiments began with a receptive field mapping stimulus consisting of a checkerboard white noise stimulus of black-and-white squares 4.3° in size, which changed at 15 Hz for 15 min. Next, mice were shown moving gratings (2, 4, and 8 Hz) that moved in eight different pseudorandomly chosen directions, in 45° intervals, at a speed of 26.6°, 53.2°, and 106.4°/s (corresponding to 800, 1600, and 3200 μm/s on the retina). Each stimulus was repeated five times.

Analysis of Neuropixels recordings

To identify DSGCs, we analyzed the response to moving gratings. gDSI and DSI were calculated as previously described. gDSI across orientations (gOSI) was calculated asgOSI $= \frac{|\Sigma R_\theta e^{2i\theta}|}{\Sigma R_\theta}$. Units with gDSI ≥ 0.15, DSI ≥ 0.3, and gDSI > gOSI and that spiked at least twice in at least three trials of the same direction, in at least one of the stimuli presented before CNO injection, were considered DS. PD was defined as the direction with the maximal response in the recording in which the response was DS. We then performed an FFT on the PSTHs of each DSGC's PD (mean PSTH over five repetitions, using 25-ms bin width) for all temporal frequencies presented and calculated the amplitude of the first harmonic at each stimulus frequency. Statistical comparison was performed with a two-way repeated-measures ANOVA with Bonferroni post hoc correction for multiple comparisons.

Only well-separated units, as determined by refractory period violations <1%, were included in our analysis. Waveforms of 100 random spikes overlaid to the mean spike shape obtained by averaging all spikes across the recording were presented for the example units. To determine RFs, the spike-triggered average (STA) from the white noise data was calculated by averaging the images that were presented in the 500 ms preceding each spike. The presented spatial RF is the result of up-sampling the STA by a factor of 4 and filtering the image with a two-dimensional (2D) Gaussian smoothing kernel.

Single-cell RNA sequencing data analysis

For the transcriptomic analysis, we assessed previously published single-cell RNA sequencing datasets from mouse retina (*37*–*39*). Raw data are available from Single Cell Portal (SCP) (*117*) or Gene Expression Omnibus accession GSE137398 (*37*), GSE81905 (*38*), GSE149715 (*39*). Cell labels and positions in the 2D t-SNE are as in the original papers. Dot plot visualizations, where color and size indicate the relative expression level across all defined clusters and the percentage of cells that expressed the gene, respectively, were generated using MATLAB custom scripts. Another mouse (*42*), a primate (*82*), and a human retina (*81*) dataset were accessed on the SCP and Human Cell Atlas (HCA) Data Explorer (*118*), respectively. Cell-type nomenclature and function were compared to other published datasets (*119*–*121*).

Quantitative OMR

The OMR was determined using the quantitative OMR system (Phenosys) as described previously (*49*, *50*, *122*). The system consists of a box whose internal walls are equipped with four screens equally spaced from an elevated central platform on which the animal is placed and is free to move. Mirrors on the floor and ceiling of the box give the optical illusion of infinite depth. An infrared camera (acquisition frame rate, 30 frames/s) is placed on the upper lid to video track on real time head movements while presenting sinusoidal vertical gratings (spatial frequency, 0.15 cycle/°) at different constant speeds (6, 12, and 35°/s) in photopic light conditions, contrast 1, rotating alternately in both directions. Each speed was randomly presented for 1 min, four to six times. The total correct and incorrect head movements with respect to the stimulus speed and direction were automatically counted by the Phenosys software based on a window of +2 to −10°/s around the stimulus speed. The OMR index was computed as the ratio of movements in the correct and incorrect direction (*49*, *123*). Sixteen C57BL/6J mice, both sexes included (11 females and 5 males), were tested in three different days in control condition (pre, treated with water), 30 min after H_1R antagonist treatment consumption (H_1R antagonist, Fenistil 1 mg/ml, GlaxoSmithKline, administered undiluted as oral drops, 10 mg/kg), and after letting them recover for at least 24 hours after the drug administration (post, treated with water). Mice were tested between 8:00 a.m. and 2:00 p.m. Statistical comparison was performed with a two-way repeated-measures ANOVA with Tukey's post hoc correction for multiple comparisons.

Human experiments

The study protocol was reviewed and approved by the Institutional Helsinki Committee of Kaplan Medical Center, Rehovot, Israel (no. 0160-19-KMC). Nine healthy men and women between the ages of 18 and 50 were recruited. All recruited participants provided signed informed consent. Exclusion criteria included chronic disease, taking regular medications, taking medication in the 2 weeks before the study visit, eye diseases that affect the functions

of the optic nerve or the retina, farsightedness or family history of narrow-angle glaucoma, difficulty urinating or known enlargement of the prostate, pregnancy, and breastfeeding. One patient was excluded from the study due to an inability to complete the study tests in light of known attention deficit hyperactivity disorder.

In this clinical, crossover, single-blind trial, each volunteer participated in two visits, at least 2 weeks apart. During one visit, 2 mg of dimetindene maleate (Fenistil, 1 mg/ml, GlaxoSmithKline) oral drops diluted in 200 ml of sweetened water was given, and during the other visit, a placebo was given. Dimetindene maleate was chosen based on safety (commonly used as an anti-allergy medication) and because it has been reported to cross the blood-brain barrier and hence would likely reach the retina (*77*, *124*). The order of the visits was random. The placebo or drug was taken between 8:00 a.m. and 12:30 p.m.; tests to assess visual function were performed 2 hours after dimetindene maleate/placebo consumption. Refraction and best-corrected visual acuity were measured in both eyes separately at the beginning of each visit, using a Snellen chart, based on autorefractometer results and an optometrist exam.

During each visit, a Heidelberg Spectralis device was used to perform macular optical coherence tomography (OCT), OCT of retinal nerve fiber layer (RNFL), and OCT angiography (OCTA) to ensure that Fenistil does not cause any morphological changes in the retina or the blood vessel density in it. We used the macular OCT and OCT RNFL images to compare the central macular thickness and mean RNFL thickness, respectively. To quantify retinal vascular density, the enface images of different vascular retinal layers obtained with OCTA were processed by ImageJ 1.52v software. Images were binarized according to Niblack's method and a grayscale mean was calculated and transformed to coverage in percentage, after subtracting the foveal avascular zone (*125*). No differences were observed between the placebo and H_1R antagonist (table S2).

Visual field tests were carried out using the Humphrey visual field analyzer (HFA). The central visual field was evaluated using the HFA 10-2 program of automated perimetry with the Swedish Interactive Threshold Algorithm (SITA) standard strategy, and the peripheral visual field was assessed using the HFA 60-4 program of automated perimetry with the SITA standard strategy. Perimetry, which refers to the systematic measurement of the visual field, measures sensitivity to stimuli at multiple locations in the visual field while monitoring fixation. Each eye is tested separately. We used a white-on-white size III (0.4 mm) target with a background luminance of 31.5 apostilbs (asb) in all the tests. The Humphrey perimeter tests light intensities over five orders of magnitudes, from 10,000 asb to 0.1 asb. Every log order change in light intensity corresponds to 10 dB, such that the machine can measure sensitivities over a 50-dB range. The SITA developed for the Humphrey perimeter estimates threshold values for each point of the visual field based on responses to stimuli presented at that location, as well as information gathered from nearby locations. In the 10-2 perimetry, 68 points in the central 10° of the visual field were measured, including the foveal sensitivity. In the 60-4 perimetry, 60 points were measured between 30° and 60° of the visual field. Fixation is assured by mapping the blind spot and then retesting the blind spot throughout the visual field test. Positive responses during retesting of the blind spot are assumed to reflect loss of fixation; the ratio between fixation losses and the number of times the blind spot was tested was less than 20% in all tests.

Statistical analysis

Statistical parameters, including the exact value of n, mean ± SD, and statistical significance, are reported in the text and figure legends. All data in the figures are presented as mean ± SEM unless otherwise indicated. The cutoff for significance was $P < 0.05$, and the significance level is marked by $^{*}P < 0.05$, $^{**}P < 0.01$, $^{***}P < 0.001$, and $^{****}P < 0.0001$. Statistical analysis was performed with MATLAB (The MathWorks Inc., Natick, MA, USA) or GraphPad software (Prism, San Diego, CA, USA). Welch's one-way ANOVA (*126*) was performed with MATLAB.

Supplementary Materials

This PDF file includes:

Figs. S1 to S8
Tables S1 and S2

REFERENCES AND NOTES

1. S. R. y Cajal, Estructura de los centros nerviosos de las aves. *Rev. Trim. Histol. Norm. Patol* **1**, 1–10 (1888).
2. S. R. y Cajal, Sur la morphologie etles connexions de larétine des oiseaux. *Anat. Anz.* **4**, 111–128 (1889).
3. J. Repérant, D. Miceli, N. P. Vesselkin, S. Molotchnikoff, The centrifugal visual system of vertebrates: A century-old search reviewed. *Int. Rev. Cytol.* **118**, 115–171 (1989).
4. U. C. Dräger, D. L. Edwards, C. J. Barnstable, Antibodies against filamentous components in discrete cell types of the mouse retina. *J. Neurosci.* **4**, 2025–2042 (1984).
5. V. H. Perry, R. Oehler, A. Cowey, Retinal ganglion cells that project to the dorsal lateral geniculate nucleus in the macaque monkey. *Neuroscience* **12**, 1101–1123 (1984).
6. M. J. Gastinger, J. J. O'Brien, N. B. Larsen, D. W. Marshak, Histamine immunoreactive axons in the macaque retina. *Invest. Ophthalmol. Vis. Sci.* **40**, 487–495 (1999).
7. M. J. Gastinger, A. J. Barber, S. A. Khin, C. S. McRill, T. W. Gardner, D. W. Marshak, Abnormal centrifugal axons in streptozotocin-diabetic rat retinas. *Invest. Ophthalmol. Vis. Sci.* **42**, 2679–2685 (2001).
8. U. Greferath, M. Kambourakis, C. Barth, E. L. Fletcher, M. Murphy, Characterization of histamine projections and their potential cellular targets in the mouse retina. *Neuroscience* **158**, 932–944 (2009).
9. K. Koves, A. Csaki, Recent research on the centrifugal visual system in mammalian species. *Anat. Physiol.* **06**, 1000216 (2016).
10. M. S. Airaksinen, P. Panula, The histaminergic system in the guinea pig central nervous system: An immunocytochemical mapping study using an antiserum against histamine. *J. Comp. Neurol.* **273**, 163–186 (1988).
11. K. A. Manning, J. R. Wilson, D. J. Uhlrich, Histamine-immunoreactive neurons and their innervation of visual regions in the cortex, tectum, and thalamus in the primate *Macaca mulatta*. *J. Comp. Neurol.* **373**, 271–282 (1996).
12. P. Panula, H. Y. Yang, E. Costa, Histamine-containing neurons in the rat hypothalamus. *Proc. Natl. Acad. Sci. U.S.A.* **81**, 2572–2576 (1984).
13. T. Watanabe, Y. Taguchi, S. Shiosaka, J. Tanaka, H. Kubota, Y. Terano, M. Tohyama, H. Wada, Distribution of the histaminergic neuron system in the central nervous system of rats; a fluorescent immunohistochemical analysis with histidine decarboxylase as a marker. *Brain Res.* **295**, 13–25 (1984).
14. M. J. Gastinger, N. Tian, T. Horvath, D. W. Marshak, Retinopetal axons in mammals: Emphasis on histamine and serotonin. *Curr. Eye Res.* **31**, 655–667 (2006).
15. L. Arbonés, J. García-Verdugo, F. Picatoste, A. García, Presence and distribution of histaminergic components in rat and bovine retina. *Neurochem. Int.* **13**, 97–104 (1988).
16. J. Z. Nowak, Histamine in the retina: Recent progress and perspectives. *Agents Actions* **30**, 202–205 (1990).
17. H. Haas, P. Panula, The role of histamine and the tuberomamillary nucleus in the nervous system. *Nat. Rev. Neurosci.* **4**, 121–130 (2003).
18. R. Frazão, D. G. McMahon, W. Schunack, P. Datta, R. Heidelberger, D. W. Marshak, Histamine elevates free intracellular calcium in mouse retinal dopaminergic cells via H1-receptors. *Invest. Ophthalmol. Vis. Sci.* **52**, 3083–3088 (2011).
19. M. J. Gastinger, A. J. Barber, N. Vardi, D. W. Marshak, Histamine receptors in mammalian retinas. *J. Comp. Neurol.* **495**, 658–667 (2006).
20. K. Horio, M. Ohkuma, E.-I. Miyachi, The effect of histamine on inward and outward currents in mouse retinal amacrine cells. *Cell. Mol. Neurobiol.* **38**, 757–767 (2018).
21. A. Vila, H. Satoh, C. Rangel, S. L. Mills, H. Hoshi, J. O'Brien, D. R. Marshak, P. R. Macleish, D. W. Marshak, Histamine receptors of cones and horizontal cells in Old World monkey retinas. *J. Comp. Neurol.* **520**, 528–543 (2012).

22. Y. Yu, H. Satoh, A. Vila, S. M. Wu, D. W. Marshak, Effects of histamine on light responses of amacrine cells in tiger salamander retina. *Neurochem. Res.* **36**, 645–654 (2011).
23. Y.-C. Yu, H. Satoh, S. M. Wu, D. W. Marshak, Histamine enhances voltage-gated potassium currents of ON bipolar cells in macaque retina. *Invest. Ophthalmol. Vis. Sci.* **50**, 959–965 (2009).
24. N. P. Akimov, D. W. Marshak, L. J. Frishman, R. D. Glickman, R. G. Yusupov, Histamine reduces flash sensitivity of on ganglion cells in the primate retina. *Invest. Ophthalmol. Vis. Sci.* **51**, 3825–3834 (2010).
25. M. J. Gastinger, R. G. Yusupov, R. D. Glickman, D. W. Marshak, The effects of histamine on rat and monkey retinal ganglion cells. *Vis. Neurosci.* **21**, 935–943 (2004).
26. H. L. Haas, O. A. Sergeeva, O. Selbach, Histamine in the nervous system. *Physiol. Rev.* **88**, 1183–1241 (2008).
27. T. E. Scammell, A. C. Jackson, N. P. Franks, W. Wisden, Y. Dauvilliers, Histamine: Neural circuits and new medications. *Sleep* **42**, zsy183 (2019).
28. K. Takahashi, J.-S. Lin, K. Sakai, Neuronal activity of histaminergic tuberomammillary neurons during wake-sleep states in the mouse. *J. Neurosci.* **26**, 10292–10298 (2006).
29. G. Vanni-Mercier, S. Gigout, G. Debilly, J. S. Lin, Waking selective neurons in the posterior hypothalamus and their response to histamine H3-receptor ligands: An electrophysiological study in freely moving cats. *Behav. Brain Res.* **144**, 227–241 (2003).
30. S. Schröder, N. A. Steinmetz, M. Krumin, M. Pachitariu, M. Rizzi, L. Lagnado, K. D. Harris, M. Carandini, Arousal modulates retinal output. *Neuron* **107**, 487–495.e9 (2020).
31. L. Liang, A. Fratzl, J. D. S. Reggiani, O. El Mansour, C. Chen, M. L. Andermann, Retinal inputs to the thalamus are selectively gated by arousal. *Curr. Biol.* **30**, 3923–3934.e9 (2020).
32. D. J. Uhlrich, K. A. Manning, J.-T. Xue, Effects of activation of the histaminergic tuberomammillary nucleus on visual responses of neurons in the dorsal lateral geniculate nucleus. *J. Neurosci.* **22**, 1098–1107 (2002).
33. X. Yu, Z. Ye, C. M. Houston, A. Y. Zecharia, Y. Ma, Z. Zhang, D. S. Uygun, S. Parker, A. L. Vyssotski, R. Yustos, N. P. Franks, S. G. Brickley, W. Wisden, Wakefulness is governed by GABA and histamine cotransmission. *Neuron* **87**, 164–178 (2015).
34. M. Greschner, G. D. Field, P. H. Li, M. L. Schiff, J. L. Gauthier, D. Ahn, A. Sher, A. M. Litke, E. J. Chichilnisky, A polyaxonal amacrine cell population in the primate retina. *J. Neurosci.* **34**, 3597–3606 (2014).
35. R. A. Warwick, N. Kaushansky, N. Sarid, A. Golan, M. Rivlin-Etzion, Inhomogeneous encoding of the visual field in the mouse retina. *Curr. Biol.* **28**, 655–665.e3 (2018).
36. A. Szél, P. Röhlich, A. R. Caffé, B. Juliusson, G. Aguirre, T. Van Veen, Unique topographic separation of two spectral classes of cones in the mouse retina. *J. Comp. Neurol.* **325**, 327–342 (1992).
37. N. M. Tran, K. Shekhar, I. E. Whitney, A. Jacobi, I. Benhar, G. Hong, W. Yan, X. Adiconis, M. E. Arnold, J. M. Lee, J. Z. Levin, D. Lin, C. Wang, C. M. Lieber, A. Regev, Z. He, J. R. Sanes, Single-cell profiles of retinal ganglion cells differing in resilience to injury reveal neuroprotective genes. *Neuron* **104**, 1039–1055.e12 (2019).
38. K. Shekhar, S. W. Lapan, I. E. Whitney, N. M. Tran, E. Z. Macosko, M. Kowalczyk, X. Adiconis, J. Z. Levin, J. Nemesh, M. Goldman, S. A. McCarroll, C. L. Cepko, A. Regev, J. R. Sanes, Comprehensive classification of retinal bipolar neurons by single-cell transcriptomics. *Cell* **166**, 1308–1323.e30 (2016).
39. W. Yan, M. A. Laboulaye, N. M. Tran, I. E. Whitney, I. Benhar, J. R. Sanes, Mouse retinal cell atlas: Molecular identification of over sixty amacrine cell types. *J. Neurosci.* **40**, 5177–5195 (2020).
40. J.-J. Pang, F. Gao, S. M. Wu, Light-evoked excitatory and inhibitory synaptic inputs to ON and OFF alpha ganglion cells in the mouse retina. *J. Neurosci.* **23**, 6063–6073 (2003).
41. M. van Wyk, H. Wässle, W. R. Taylor, Receptive field properties of ON- and OFF-ganglion cells in the mouse retina. *Vis. Neurosci.* **26**, 297–308 (2009).
42. E. Z. Macosko, A. Basu, R. Satija, J. Nemesh, K. Shekhar, M. Goldman, I. Tirosh, A. R. Bialas, N. Kamitaki, E. M. Martersteck, J. J. Trombetta, D. A. Weitz, J. R. Sanes, A. K. Shalek, A. Regev, S. A. McCarroll, Highly parallel genome-wide expression profiling of individual cells using nanoliter droplets. *Cell* **161**, 1202–1214 (2015).
43. M. J. McGinley, M. Vinck, J. Reimer, R. Batista-Brito, E. Zagha, C. R. Cadwell, A. S. Tolias, J. A. Cardin, D. A. McCormick, Waking state: Rapid variations modulate neural and behavioral responses. *Neuron* **87**, 1143–1161 (2015).
44. G. M. Alexander, S. C. Rogan, A. I. Abbas, B. N. Armbruster, Y. Pei, J. A. Allen, R. J. Nonneman, J. Hartmann, S. S. Moy, M. A. Nicolelis, J. O. McNamara, B. L. Roth, Remote control of neuronal activity in transgenic mice expressing evolved G protein-coupled receptors. *Neuron* **63**, 27–39 (2009).
45. B. N. Armbruster, X. Li, M. H. Pausch, S. Herlitze, B. L. Roth, Evolving the lock to fit the key to create a family of G protein-coupled receptors potently activated by an inert ligand. *Proc. Natl. Acad. Sci. U.S.A.* **104**, 5163–5168 (2007).
46. S. C. Rogan, B. L. Roth, Remote control of neuronal signaling. *Pharmacol. Rev.* **63**, 291–315 (2011).
47. M. M. Roth, J. C. Dahmen, D. R. Muir, F. Imhof, F. J. Martini, S. B. Hofer, Thalamic nuclei convey diverse contextual information to layer 1 of visual cortex. *Nat. Neurosci.* **19**, 299–307 (2016).
48. O. S. Dhande, M. E. Estevez, L. E. Quattrochi, R. N. El-Danaf, P. L. Nguyen, D. M. Berson, A. D. Huberman, Genetic dissection of retinal inputs to brainstem nuclei controlling image stabilization. *J. Neurosci.* **33**, 17797–17813 (2013).
49. F. Kretschmer, V. Kretschmer, V. P. Kunze, J. Kretzberg, OMR-arena: Automated measurement and stimulation system to determine mouse visual thresholds based on optomotor responses. *PLOS ONE* **8**, e78058 (2013).
50. F. Kretschmer, M. Tariq, W. Chatila, B. Wu, T. C. Badea, Comparison of optomotor and optokinetic reflexes in mice. *J. Neurophysiol.* **118**, 300–316 (2017).
51. F. M. Honrubia, J. H. Elliott, Efferent innervation of the retina. I. Morphologic study of the human retina. *Arch. Ophthalmol.* **80**, 98–103 (1968).
52. J. A. Osterhout, B. K. Stafford, P. L. Nguyen, Y. Yoshihara, A. D. Huberman, Contactin-4 mediates axon-target specificity and functional development of the accessory optic system. *Neuron* **86**, 985–999 (2015).
53. M. Monnier, R. Sauer, A. M. Hatt, The activating effect of histamine on the central nervous system. *Int. Rev. Neurobiol.* **12**, 265–305 (1970).
54. H. Wada, N. Inagaki, A. Yamatodani, T. Watanabe, Is the histaminergic neuron system a regulatory center for whole-brain activity? *Trends Neurosci.* **14**, 415–418 (1991).
55. S. Erisken, A. Vaiceliunaite, O. Jurjut, M. Fiorini, S. Katzner, L. Busse, Effects of locomotion extend throughout the mouse early visual system. *Curr. Biol.* **24**, 2899–2907 (2014).
56. Ç. Aydın, J. Couto, M. Giugliano, K. Farrow, V. Bonin, Locomotion modulates specific functional cell types in the mouse visual thalamus. *Nat. Commun.* **9**, 4882 (2018).
57. S. Ito, D. A. Feldheim, A. M. Litke, Segregation of visual response properties in the mouse superior colliculus and their modulation during locomotion. *J. Neurosci.* **37**, 8428–8443 (2017).
58. C. M. Niell, M. P. Stryker, Modulation of visual responses by behavioral state in mouse visual cortex. *Neuron* **65**, 472–479 (2010).
59. C. Stringer, M. Pachitariu, N. Steinmetz, C. B. Reddy, M. Carandini, K. D. Harris, Spontaneous behaviors drive multidimensional, brainwide activity. *Science* **364**, 255 (2019).
60. M. Vinck, R. Batista-Brito, U. Knoblich, J. A. Cardin, Arousal and locomotion make distinct contributions to cortical activity patterns and visual encoding. *Neuron* **86**, 740–754 (2015).
61. E. L. Savier, H. Chen, J. Cang, Effects of locomotion on visual responses in the mouse superior colliculus. *J. Neurosci.* **39**, 9360–9368 (2019).
62. P. J. Mineault, E. Tring, J. T. Trachtenberg, D. L. Ringach, Enhanced spatial resolution during locomotion and heightened attention in mouse primary visual cortex. *J. Neurosci.* **36**, 6382–6392 (2016).
63. R. S. Williamson, K. E. Hancock, B. G. Shinn-Cunningham, D. B. Polley, Locomotion and task demands differentially modulate thalamic audiovisual processing during active search. *Curr. Biol.* **25**, 1885–1891 (2015).
64. E. M. Ellis, G. Gauvain, B. Sivyer, G. J. Murphy, Shared and distinct retinal input to the mouse superior colliculus and dorsal lateral geniculate nucleus. *J. Neurophysiol.* **116**, 602–610 (2016).
65. C. Chen, W. G. Regehr, Presynaptic modulation of the retinogeniculate synapse. *J. Neurosci.* **23**, 3130–3135 (2003).
66. D. P. Seeburg, X. Liu, C. Chen, Frequency-dependent modulation of retinogeniculate transmission by serotonin. *J. Neurosci.* **24**, 10950–10962 (2004).
67. Y. W. Lam, S. M. Sherman, Activation of both Group I and Group II metabotropic glutamatergic receptors suppress retinogeniculate transmission. *Neuroscience* **242**, 78–84 (2013).
68. Y.-C. Yang, C.-C. Hu, C.-S. Huang, P.-Y. Chou, Thalamic synaptic transmission of sensory information modulated by synergistic interaction of adenosine and serotonin. *J. Neurochem.* **128**, 852–863 (2014).
69. E. M. Martersteck, K. E. Hirokawa, M. Evarts, A. Bernard, X. Duan, Y. Li, L. Ng, S. W. Oh, B. Ouellette, J. J. Royall, M. Stoecklin, Q. Wang, H. Zeng, J. R. Sanes, J. A. Harris, Diverse central projection patterns of retinal ganglion cells. *Cell Rep.* **18**, 2058–2072 (2017).
70. L. P. Morin, K. M. Studholme, Retinofugal projections in the mouse. *J. Comp. Neurol.* **522**, 3733–3753 (2014).
71. W. Wei, Neural mechanisms of motion processing in the mammalian retina. *Annu. Rev. Vis. Sci.* **4**, 165–192 (2018).
72. L. Ankri, E. Ezra-Tsur, S. R. Maimon, N. Kaushansky, M. Rivlin-Etzion, Antagonistic center-surround mechanisms for direction selectivity in the retina. *Cell Rep.* **31**, 107608 (2020).
73. J. L. Gomez, J. Bonaventura, W. Lesniak, W. B. Mathews, P. Sysa-Shah, L. A. Rodriguez, R. J. Ellis, C. T. Richie, B. K. Harvey, R. F. Dannals, M. G. Pomper, A. Bonci, M. Michaelides, Chemogenetics revealed: DREADD occupancy and activation via converted clozapine. *Science* **357**, 503–507 (2017).
74. M. Jendryka, M. Palchaudhuri, D. Ursu, B. van der Veen, B. Liss, D. Kätzel, W. Nissen, A. Pekcec, Pharmacokinetic and pharmacodynamic actions of clozapine-N-oxide, clozapine, and compound 21 in DREADD-based chemogenetics in mice. *Sci. Rep.* **9**, 4522 (2019).

75. G. Drutel, N. Peitsaro, K. Karlstedt, K. Wieland, M. J. Smit, H. Timmerman, P. Panula, R. Leurs, Identification of rat H3 receptor isoforms with different brain expression and signaling properties. *Mol. Pharmacol.* **59**, 1–8 (2001).
76. S. Morisset, A. Rouleau, X. Ligneau, F. Gbahou, J. Tardivel-Lacombe, H. Stark, W. Schunack, C. R. Ganellin, J. C. Schwartz, J. M. Arrang, High constitutive activity of native H3 receptors regulates histamine neurons in brain. *Nature* **408**, 860–864 (2000).
77. A. M. Mahdy, N. R. Webster, Histamine and antihistamines. *Anaesth. Intens. Care Medicine* **18**, 210–215 (2017).
78. P. Turner, Critical flicker frequency and centrally-acting drugs. *Br. J. Ophthalmol.* **52**, 245–250 (1968).
79. A. N. Nicholson, P. A. Smith, M. B. Spencer, Antihistamines and visual function: Studies on dynamic acuity and the pupillary response to light. *Br. J. Clin. Pharmacol.* **14**, 683–690 (1982).
80. A. N. Nicholson, B. M. Stone, The H1-antagonist mequitazine: Studies on performance and visual function. *Eur. J. Clin. Pharmacol.* **25**, 563–566 (1983).
81. J. Li, J. Wang, I. L. Ibarra, X. Cheng, M. D. Luecken, J. Lu, A. Monavarfeshani, W. Yan, Y. Zheng, Z. Zuo, S. L. Z. Colborn, B. S. Cortez, L. A. Owen, N. M. Tran, K. Shekhar, J. R. Sanes, J. T. Stout, S. Chen, Y. Li, M. M. DeAngelis, F. J. Theis, R. Chen, Integrated multi-omics single cell atlas of the human retina. *Res. Sq.* (2023) doi: 10.21203/rs.3.rs-3471275/v1.
82. Y.-R. Peng, K. Shekhar, W. Yan, D. Herrmann, A. Sappington, G. S. Bryman, T. van Zyl, M. T. H. Do, A. Regev, J. R. Sanes, Molecular classification and comparative taxonomics of foveal and peripheral cells in primate retina. *Cell* **176**, 1222–1237.e22 (2019).
83. S. K. Itaya, P. W. Itaya, Centrifugal fibers to the rat retina from the medial pretectal area and the periaqueductal grey matter. *Brain Res.* **326**, 362–365 (1985).
84. J. L. Labandeira-Garcia, M. J. Guerra-Seijas, F. Gonzalez, R. Perez, C. Acuña, Location of neurons projecting to the retina in mammals. *Neurosci. Res.* **8**, 291–302 (1990).
85. M. J. Villar, M. L. Vitale, M. N. Parisi, Dorsal raphe serotonergic projection to the retina. A combined peroxidase tracing-neurochemical/high-performance liquid chromatography study in the rat. *Neuroscience* **22**, 681–686 (1987).
86. N. Bons, A. Petter, Retinal afferents of hypothalamic origin in a prosimian primate: Microcebus murinus. Study using retrograde fluorescent tracers. *C. R. Acad. Sci. III* **303**, 719–722 (1986).
87. H. Terubayashi, H. Fujisawa, M. Itoi, Y. Ibata, Hypothalamo-retinal centrifugal projection in the dog. *Neurosci. Lett.* **40**, 1–6 (1983).
88. J. N. Larsen, M. Møller, Evidence for efferent projections from the brain to the retina of the Mongolian gerbil (*Meriones unguiculatus*). A horseradish peroxidase tracing study. *Acta. Ophthalmol. Suppl.* **173**, 11–14 (1985).
89. P. V. Hoogland, A. Vanderkrans, F. D. Koole, H. J. Groenewegen, A direct projection from the nucleus oculomotorius to the retina in rats. *Neurosci. Lett.* **56**, 323–328 (1985).
90. J. Repérant, The orthograde transport of horseradish peroxidase in the visual system. *Brain Res.* **85**, 307–312 (1975).
91. H. Schnyder, H. Künzle, Is there a retinopetal system in the rat? *Exp. Brain Res.* **56**, 502–508 (1984).
92. J. N. Davis, P. N. McKinnon, Anterograde and transcellular transport of a fluorescent dye, bisbenzimide, in the rat visual system. *Neurosci. Lett.* **29**, 207–212 (1982).
93. C. Weidner, D. Miceli, J. Repérant, Orthograde axonal and transcellular transport of different fluorescent tracers in the primary visual system of the rat. *Brain Res.* **272**, 129–136 (1983).
94. M. Schütte, Centrifugal innervation of the rat retina. *Vis. Neurosci.* **12**, 1083–1092 (1995).
95. J. Repérant, S. Araneda, D. Miceli, M. Medina, J. P. Rio, Serotonergic retinopetal projections from the dorsal raphe nucleus in the mouse demonstrated by combined [^{3}H] 5-HT retrograde tracing and immunolabeling of endogenous 5-HT. *Brain Res.* **878**, 213–217 (2000).
96. M. J. Gastinger, A. S. Bordt, M. P. Bernal, D. W. Marshak, Serotonergic retinopetal axons in the monkey retina. *Curr. Eye Res.* **30**, 1089–1095 (2005).
97. M. Rivlin-Etzion, K. Zhou, W. Wei, J. Elstrott, P. L. Nguyen, B. A. Barres, A. D. Huberman, M. B. Feller, Transgenic mice reveal unexpected diversity of on-off direction-selective retinal ganglion cell subtypes and brain structures involved in motion processing. *J. Neurosci.* **31**, 8760–8769 (2011).
98. H. Dana, T.-W. Chen, A. Hu, B. C. Shields, C. Guo, L. L. Looger, D. S. Kim, K. Svoboda, Thy1-GCaMP6 transgenic mice for neuronal population imaging in vivo. *PLOS ONE* **9**, e108697 (2014).
99. A. Y. Zecharia, X. Yu, T. Götz, Z. Ye, D. R. Carr, P. Wulff, B. Bettler, A. L. Vyssotski, S. G. Brickley, N. P. Franks, W. Wisden, GABAergic inhibition of histaminergic neurons regulates active waking but not the sleep-wake switch or propofol-induced loss of consciousness. *J. Neurosci.* **32**, 13062–13075 (2012).
100. S. Gong, M. Doughty, C. R. Harbaugh, A. Cummins, M. E. Hatten, N. Heintz, C. R. Gerfen, Targeting Cre recombinase to specific neuron populations with bacterial artificial chromosome constructs. *J. Neurosci.* **27**, 9817–9823 (2007).
101. S. Gong, C. Zheng, M. L. Doughty, K. Losos, N. Didkovsky, U. B. Schambra, N. J. Nowak, A. Joyner, G. Leblanc, M. E. Hatten, N. Heintz, A gene expression atlas of the central nervous system based on bacterial artificial chromosomes. *Nature* **425**, 917–925 (2003).
102. J. Schindelin, I. Arganda-Carreras, E. Frise, V. Kaynig, M. Longair, T. Pietzsch, S. Preibisch, C. Rueden, S. Saalfeld, B. Schmid, J.-Y. Tinevez, D. J. White, V. Hartenstein, K. Eliceiri, P. Tomancak, A. Cardona, Fiji: An open-source platform for biological-image analysis. *Nat. Methods* **9**, 676–682 (2012).
103. P. Bankhead, M. B. Loughrey, J. A. Fernández, Y. Dombrowski, D. G. McArt, P. D. Dunne, S. McQuaid, R. T. Gray, L. J. Murray, H. G. Coleman, J. A. James, M. Salto-Tellez, P. W. Hamilton, QuPath: Open source software for digital pathology image analysis. *Sci. Rep.* **7**, 16878 (2017).
104. W. Wei, J. Elstrott, M. B. Feller, Two-photon targeted recording of GFP-expressing neurons for light responses and live-cell imaging in the mouse retina. *Nat. Protoc.* **5**, 1347–1352 (2010).
105. D. Karamanlis, T. Gollisch, Nonlinear spatial integration underlies the diversity of retinal ganglion cell responses to natural images. *J. Neurosci.* **41**, 3479–3498 (2021).
106. D. H. Brainard, The psychophysics toolbox. *Spat. Vis.* **10**, 433–436 (1997).
107. D. G. Pelli, The VideoToolbox software for visual psychophysics: Transforming numbers into movies. *Spat. Vis.* **10**, 437–442 (1997).
108. B. G. Borghuis, J. S. Marvin, L. L. Looger, J. B. Demb, Two-photon imaging of nonlinear glutamate release dynamics at bipolar cell synapses in the mouse retina. *J. Neurosci.* **33**, 10972–10985 (2013).
109. C. A. Schneider, W. S. Rasband, K. W. Eliceiri, NIH Image to ImageJ: 25 years of image analysis. *Nat. Methods* **9**, 671–675 (2012).
110. M. Pachitariu, N. Steinmetz, S. Kadir, M. Carandini, K. D. Harris, Kilosort: Realtime spike-sorting for extracellular electrophysiology with hundreds of channels. bioRxiv 061481 [Preprint] (2016). https://doi.org/10.1101/061481.
111. M. Pachitariu, N. A. Steinmetz, J. Colonell, Kilosort2 (2018); https://github.com/MouseLand/.
112. C. Rossant, S. N. Kadir, D. F. M. Goodman, J. Schulman, M. L. D. Hunter, A. B. Saleem, A. Grosmark, M. Belluscio, G. H. Denfield, A. S. Ecker, A. S. Tolias, S. Solomon, G. Buzsaki, M. Carandini, K. D. Harris, Spike sorting for large, dense electrode arrays. *Nat. Neurosci.* **19**, 634–641 (2016).
113. C. Rossant, K. D. Harris, Hardware-accelerated interactive data visualization for neuroscience in Python. *Front. Neuroinform.* **7**, 36 (2013).
114. R. Segev, J. Goodhouse, J. Puchalla, M. J. Berry II, Recording spikes from a large fraction of the ganglion cells in a retinal patch. *Nat. Neurosci.* **7**, 1155–1162 (2004).
115. J. J. Jun, N. A. Steinmetz, J. H. Siegle, D. J. Denman, M. Bauza, B. Barbarits, A. K. Lee, C. A. Anastassiou, A. Andrei, Ç. Aydın, M. Barbic, T. J. Blanche, V. Bonin, J. Couto, B. Dutta, S. L. Gratiy, D. A. Gutnisky, M. Häusser, B. Karsh, P. Ledochowitsch, C. M. Lopez, C. Mitelut, S. Musa, M. Okun, M. Pachitariu, J. Putzeys, P. D. Rich, C. Rossant, W.-L. Sun, K. Svoboda, M. Carandini, K. D. Harris, C. Koch, J. O'Keefe, T. D. Harris, Fully integrated silicon probes for high-density recording of neural activity. *Nature* **551**, 232–236 (2017).
116. P. Shamash, M. Carandini, K. D. Harris, N. A. Steinmetz, A tool for analyzing electrode tracks from slice histology. bioRxiv 10.1101/447995 (2018).
117. SCP, Broad Institute, Single cell portal; https://singlecell.broadinstitute.org/single_cell.
118. HCA Data Explorer, The human cell atlas; https://data.humancellatlas.org/.
119. W. Huang, Q. Xu, J. Su, L. Tang, Z.-Z. Hao, C. Xu, R. Liu, Y. Shen, X. Sang, N. Xu, X. Tie, Z. Miao, X. Liu, Y. Xu, F. Liu, Y. Liu, S. Liu, Linking transcriptomes with morphological and functional phenotypes in mammalian retinal ganglion cells. *Cell Rep.* **40**, 111322 (2022).
120. J. Goetz, Z. F. Jessen, A. Jacobi, A. Mani, S. Cooler, D. Greer, S. Kadri, J. Segal, K. Shekhar, J. R. Sanes, G. W. Schwartz, Unified classification of mouse retinal ganglion cells using function, morphology, and gene expression. *Cell Rep.* **40**, 111040 (2022).
121. A. Y. M. Wang, M. M. Kulkarni, A. J. McLaughlin, J. Gayet, B. E. Smith, M. Hauptschein, C. F. McHugh, Y. Y. Yao, T. Puthussery, An ON-type direction-selective ganglion cell in primate retina. *Nature* **623**, 381–386 (2023).
122. F. Kretschmer, S. Sajgo, V. Kretschmer, T. C. Badea, A system to measure the optokinetic and optomotor response in mice. *J. Neurosci. Methods* **256**, 91–105 (2015).
123. S. Francia, D. Shmal, S. Di Marco, G. Chiaravalli, J. F. Maya-Vetencourt, G. Mantero, C. Michetti, S. Cupini, G. Manfredi, M. L. DiFrancesco, A. Rocchi, S. Perotto, M. Attanasio, R. Sacco, S. Bisti, M. Mete, G. Pertile, G. Lanzani, E. Colombo, F. Benfenati, Light-induced charge generation in polymeric nanoparticles restores vision in advanced-stage retinitis pigmentosa rats. *Nat. Commun.* **13**, 3677 (2022).
124. S. Noguchi, T. Inukai, T. Kuno, C. Tanaka, The suppression of olfactory bulbectomy-induced muricide by antidepressants and antihistamines via histamine H1 receptor blocking. *Physiol. Behav.* **51**, 1123–1127 (1992).
125. A. Fujiwara, Y. Morizane, M. Hosokawa, S. Kimura, Y. Shiode, M. Hirano, S. Doi, S. Toshima, K. Takahashi, M. Hosogi, F. Shiraga, Factors affecting foveal avascular zone in healthy eyes: An examination using swept-source optical coherence tomography angiography. *PLOS ONE* **12**, e0188572 (2017).
126. A. Penn, MATLAB Central File Exchange, wanova (2021); https://mathworks.com/matlabcentral/fileexchange/61661-wanova.

Acknowledgments: We thank H. Voet for statistical consultation, M. Groysman for custom viral production, M. Shein-Idelson for sharing the framework for the visual stimulation graphical user interface, M. Oren-Suissa for using her confocal microscope, E. Solomon for help with histology, and members of the Gollisch laboratory for helpful advice about MEA recordings. **Funding:** This work was supported by research grants from the European Research Council (ERC starter no. 757732), the Israel Science Foundation (2449/20), the Minerva Foundation with funding from the Federal German Ministry for Education and Research, the Charles and David Wolfson Charitable Trust, the Rolf Wiklund and Alice Wiklund Parkinson's Disease Research Fund, the Consolidated Anti-Aging Foundation, and D. C. Andreae. A.S.H. was supported by the Minerva Fellowship, L.A. was supported by ISEF, S.R. was supported by a Dean Fellowship of the Weizmann Institute of Science, and M.R.-E. is incumbent of the Sara Lee Schupf Family Chair. **Author contributions:** Conceptualization: M.R.-E., R.A.W., and S.R. Methodology: M.R.-E., R.A.W., S.R., A.S.H., H.Y., N.G., and S.D.M. Investigation: R.A.W., S.R., A.S.H., H.Y., B.P.S., L.A., and N.G. Data analysis: R.A.W., S.R., A.S.H., L.A., and J.M. Visualization: R.A.W., S.R., and A.S.H. Supervision: M.R.-E. and R.P.-Y. Writing—original draft: M.R.-E., R.A.W., and S.R. Writing—review and editing: M.R.-E., R.A.W., S.R., N.G., A.S.H., H.Y., B.P.S., L.A., and R.P.-Y. **Competing interests:** The authors declare that they have no competing interests. **Data and materials availability:** All data needed to evaluate the conclusions in the paper are present in the paper and/or the Supplementary Materials. Data and the code to produce the figures are available at https://zenodo.org/records/11198169.

Submitted 21 August 2023
Accepted 24 July 2024
Published 28 August 2024
10.1126/sciadv.adk4062